

AEROSOL DEPOSITION IN TRANSPORT LINES

A Dissertation

by

ARNOLDO MUYSHONDT

**Submitted to the Office of Graduate Studies of
Texas A&M University
in partial fulfillment of the requirements for the degree of**

DOCTOR OF PHILOSOPHY

December 1995

Major Subject: Mechanical Engineering

UMI Number: 9615852

UMI Microform 9615852
Copyright 1996, by UMI Company. All rights reserved.

**This microform edition is protected against unauthorized
copying under Title 17, United States Code.**

UMI
300 North Zeeb Road
Ann Arbor, MI 48103

AEROSOL DEPOSITION IN TRANSPORT LINES

A Dissertation

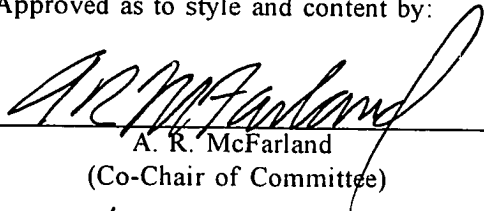
by

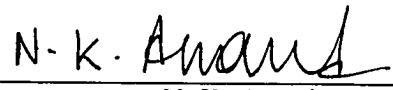
ARNOLDO MUYSHONDT

Submitted to Texas A&M University
in partial fulfillment of the requirements
for the degree of

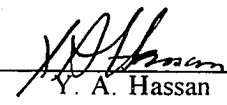
DOCTOR OF PHILOSOPHY


Approved as to style and content by:



A. R. McFarland
(Co-Chair of Committee)


N. K. Anand
(Co-Chair of Committee)


K. D. Kihm
(Member)


Y. A. Hassan
(Member)


W. H. Marlow
(Member)


G. P. Peterson
(Head of Department)

December 1995

Major Subject: Mechanical Engineering

ABSTRACT

Aerosol Deposition in Transport Lines. (December 1995)

Arnoldo Muyshondt, B. S., Texas Tech University;

M. S., Texas Tech University

Co-Chairs of Advisory Committee: Dr. A. R. McFarland
Dr. N. K. Anand

Particle deposition in contraction fittings with half-angles of 12°, 45°, and 90°; expansion fittings with half-angles of 3°, 6°, 12°, 45°, and 90°; and large-diameter transport lines (up to 102 mm diameter) was measured experimentally. Aerosol losses in the transition fittings were found to be a function of three parameters; namely, Stokes number, area ratio, and half-angle. Based on experimental data, correlations were developed that allow prediction of particle losses in contraction and expansion fittings as a function of Stokes number, area ratio, and half-angle. A correlation was also developed for large transport tubes that allows prediction of non-dimensional deposition velocity as a function of non-dimensional relaxation time and flow Reynolds number.

For a given half-angle, losses in a contraction fitting correlate well with the parameter $Stk_c (1-A_o/A_c)$. Aerosol particle deposition in the contraction fittings was also modelled numerically and the numerical results show good agreement with experimental data. In general, losses in a contraction fitting decrease with decreasing half-angle and area ratio.

Losses in expansion fittings increase with decreasing half-angle down to an angle of approximately 12°; thereafter, losses decrease with decreasing half-angle. Losses decrease with decreasing area ratio. A 90° expansion half-angle fitting produced the lowest aerosol losses.

The correlation for large-diameter transport tubes shows good agreement with previous correlations for deposition in small diameter tubes as well for the full range of tube sizes (13 mm to 102 mm diameter) and Reynolds numbers (up to 55,000) tested. For large tubes, the correlation shows improved prediction characteristics as compared to earlier models. For example, penetration of 20 μm aerodynamic diameter aerosol particles through a 102 mm diameter tube at a flow rate of 2260 L/min was measured to be 59%. The present model predicts a penetration of 62%, while two previously reported models that do not include Reynolds number effects, predict 80% and 82%.

The correlations presented in this study should be useful sub-models for predicting aerosol losses in transition fittings and large-diameter transport systems; in general, models that are used to evaluate overall losses in aerosol transport systems.

ACKNOWLEDGEMENTS

Funding for this project was provided by the U. S. Nuclear Regulatory Commission (NRC) under the supervision of Dr. S. A. McGuire (Grant Nos. NRC-04-92-080 and NRC-04-94-099). The financial and technical support of NRC and Dr. McGuire are gratefully acknowledged.

I would like to express my thanks to Dr. A. R. McFarland and Dr. N. K. Anand; their guidance, advice, and sponsorship made it possible for me to complete this study.

Many thanks to Dr. K. D. Kihm, Dr. Y. A. Hassan, and Dr. W. H. Marlow for their time spent reviewing this work as members of my graduate committee.

My appreciation goes to Carlos Ortiz for his advice and help in completing all the experiments presented in this study. Many thanks to all the students at the Aerosol Technology Laboratory.

Finally, I dedicate this work to my wife, parents, and family; their love, support, and understanding made it all much easier.

TABLE OF CONTENTS

	Page
ABSTRACT	iii
ACKNOWLEDGEMENTS	v
TABLE OF CONTENTS	vi
LIST OF FIGURES	viii
LIST OF TABLES	xi
LIST OF SYMBOLS	xii
CHAPTER	
I INTRODUCTION	1
II LITERATURE SURVEY	6
III NUMERICAL PROCEDURE	12
IV EXPERIMENTAL PROCEDURES	18
V CONTRACTION FITTINGS	25
VI EXPANSION FITTINGS	38
VII LARGE-DIAMETER TRANSPORT TUBES	49
VII SUMMARY	65
REFERENCES	67
APPENDIX A	71
APPENDIX B	78
APPENDIX C	83

	Page
APPENDIX D	87
APPENDIX E	91
APPENDIX F	97
VITA	102

LIST OF FIGURES

Figure	Page
1.1 Comparison of conventional and large transport line sampling systems.	3
3.1 Sample computational mesh, velocity vectors, and streamlines for a contraction fitting.	13
4.1 Schematic of transition fittings.	19
4.2 Experimental setup for testing contraction fittings.	20
4.3 Experimental setup for testing expansion fittings.	21
4.4 Experimental setup for testing large transport tubes.	22
5.1 Wall loss for 90° contraction fittings.	26
5.2 Wall loss for 45° contraction fittings.	27
5.3 Wall loss for 12° contraction fittings.	28
5.4 Correlation surface for contraction fittings.	31
5.5 Comparison of aerosol particle losses for a 90° contraction fitting predicted by Equation 5.2 and the model of Pich (1964), Ye and Pui (1990), and Chen and Pui (1995).	32
5.6 Comparison of aerosol particle losses for a 45° contraction fitting predicted by Equation 5.2 and the model of Chen and Pui (1995).	35
5.7 Comparison of aerosol particle losses for a 12° contraction fitting predicted by Equation 5.2 and the model of Chen and Pui (1995).	36

Figure	Page
6.1 Wall loss for 3° expansion fitting.	39
6.2 Wall loss for 6° expansion fittings.	40
6.3 Wall loss for 12° expansion fittings.	41
6.4 Wall loss for 45° expansion fittings.	42
6.5 Wall loss for 90° expansion fittings.	43
6.6 Wall loss for expansion fittings as predicted by Equation 6.2, $A_o/A_e = 1.7$	45
6.7 Wall loss for expansion fittings as predicted by Equation 6.2, $A_o/A_e = 4$	46
6.8 Wall loss for expansion fittings as predicted by Equation 6.2, $A_o/A_e = 16$	47
7.1 Non-dimensional deposition velocity as a function of non-dimensional particle relaxation time for various tube diameters.	50
7.2 Correlation surface for large-diameter transport tubes.	53
7.3 Non-dimensional deposition velocity as a function of non-dimensional particle relaxation time for constant Reynolds numbers.	54
7.4 Penetration of 10 μm AD aerosol particles through a 13 mm diameter by 2.7 m long vertical tube.	55
7.5 Penetration of 20 μm AD aerosol particles through a 26 mm diameter by 2.7 m long vertical tube.	56

Figure	Page
7.6 Penetration of 20 μm AD aerosol particles through a 52 mm diameter by 2.7 m long vertical tube.	57
7.7 Penetration of 20 μm AD aerosol particles through a 102 mm diameter by 5.5 m long vertical tube.	58
A.1 Extension pieces used for testing expansion and contraction fittings. . . .	72
A.2 Detailed drawings for the 90° fittings.	73
A.3 Detailed drawings for the 45° fittings.	74
A.4 Detailed drawings for the 12° fittings.	75
A.5 Detailed drawings for the 6° fittings.	76
A.6 Detailed drawings for the 3° fittings.	77

LIST OF TABLES

Table	Page
2.1 Previous Work on Particle Deposition in Vertical Tubes.	8
3.1 Grid Independance Study.	16
C.1 Experimental Data for 90° Contraction Fittings.	84
C.2 Experimental Data for 45° Contraction Fittings.	85
C.3 Experimental Data for 12° Contraction Fittings.	86
D.1 Numerical Data for 90° Contraction Fittings.	88
D.2 Numerical Data for 45° Contraction Fittings.	89
D.3 Numerical Data for 12° Contraction Fittings.	90
E.1 Experimental Data for 90° Expansion Fittings.	92
E.2 Experimental Data for 45° Expansion Fittings.	93
E.3 Experimental Data for 12° Expansion Fittings.	94
E.4 Experimental Data for 6° Expansion Fittings.	95
E.5 Experimental Data for 3° Expansion Fittings.	96
F.1 Experimental Data for a 13 mm ID and 2.7 m Long Transport Tube. . .	98
F.2 Experimental Data for a 26 mm ID and 2.7 m Long Transport Tube. . .	99
F.3 Experimental Data for a 52 mm ID and 2.7 m Long Transport Tube. . .	100
F.4 Experimental Data for a 102 mm ID and 5.5 m Long Transport Tube. . .	101

LIST OF SYMBOLS

A_e	=	Entrance cross-sectional area
A_o	=	Outlet cross-sectional area
B_i	=	Bias limit of measurement
C_o	=	Cunningham's slip correction factor based on D_a
C_c	=	Cunningham's slip correction factor
C_D	=	Particle drag coefficient
c_{dn}	=	Outlet plane aerosol concentration
C_p	=	Cunningham's slip correction factor based on D_p
c_{up}	=	Entrance plane aerosol concentration
D_a	=	Particle mean aerodynamic diameter
d_e	=	Entrance duct diameter
d_o	=	Outlet duct diameter
D_p	=	Aerosol particle diameter
d_t	=	Duct diameter
f	=	Friction factor
f_f	=	Flattening factor
f_{Lr}	=	Radial component of the Saffman force
f_{Lz}	=	Axial component of the Saffman force
g	=	Gravitational acceleration
G_i	=	Average value of independent parameter

k_+	=	Non-dimensional surface roughness
K_+	=	Non-dimensional particle transport coefficient
K_b	=	Boltzman's constant
L	=	Duct length
L_+	=	Non-dimensional lift force
P	=	Aerosol particle penetration
Q	=	Flow rate
R	=	Result value
R_+	=	Non-dimensional particle radius
Re	=	Reynolds number based on duct diameter
r_p	=	Particle radial displacement
S_+	=	Non-dimensional stopping distance
Sc	=	Schmidt number
S_i	=	Standard deviation of measurement
Stk_c	=	Contraction fitting Stokes number
Stk_e	=	Expansion fitting Stokes number
t	=	Time
T	=	Temperature
u	=	Gas radial velocity component
U	=	Duct mean velocity
U	=	Gas instantaneous velocity vector
u'	=	Gas fluctuating velocity vector
\bar{u}	=	Average gas velocity vector

U_e	=	Contraction or expansion fitting entrance velocity
U_n	=	Uncertainty
U_o	=	Contraction or expansion fitting outlet velocity
u_p	=	Particle radial velocity component
U_p	=	Particle instantaneous velocity vector
v	=	Gas tangential velocity component
v_+	=	Non-dimensional deposition velocity
v'	=	R. m. s. radial velocity fluctuation component
v'_+	=	Non-dimensional r. m. s. radial velocity fluctuation component
V_*	=	Friction velocity
Vb_+	=	Non-dimensional Brownian diffusion velocity
V_d	=	Deposition velocity
v_p	=	Particle tangential velocity component
Vs_+	=	Non-dimensional particle coasting velocity
w	=	Gas axial velocity component
Wl	=	Wall loss
w_p	=	Particle axial velocity component
y_+	=	Non-dimensional distance from the wall
z_p	=	Particle axial displacement
θ	=	Contraction or expansion fitting half angle
θ_p	=	Particle tangential displacement
δ	=	Sensitivity parameter
μ	=	Viscosity of air

- ν = Kinematic viscosity of air
- ρ_p = Aerosol particle density
- σ_g = Geometric standard deviation
- τ = Particle relaxation time
- τ_+ = Non-dimensional particle relaxation time

CHAPTER I

INTRODUCTION

The Environmental Protection Agency (EPA) has promulgated rules for continuous emissions monitoring (CEM) of stacks and ducts in nuclear facilities where there is a potential of significant emissions of radionuclides (U.S. EPA, 1994a and 1994b). The United States Congress has also mandated that rules be setup by EPA for CEM of non-nuclear incinerators that process over 250 tons/year (*U.S. Statutes at Large*, 1990). EPA stipulates that nuclear CEM shall be performed following the methodology outlined under ANSI Standard N13.1-1969 (ANSI, 1969), which requires evaluation of aerosol losses in transport lines. Recently, EPA has granted the U. S. Department of Energy (DOE) permission to use Alternate Reference Methodologies (ARM) for sampling at its facilities in place of the ANSI N13.1-1969 standard (U. S. EPA, 1994c). The ARM as well as the Nuclear Regulatory Commission (NRC) recommend the use of the DEPOSITION code (Anand, 1993) for the evaluation of sampling line aerosol losses. For any extractive means of sampling, it is important that the transport line losses are minimized, not only to ensure a representative sample at the collection or analysis section, but also to minimize the need for cleaning of the transport system.

A general aerosol stack sampling system consists of a sampling probe, horizontal and vertical straight tubes, elbows (bends), and in many situations, contraction and

Format follows the style of *Aerosol Science and Technology Journal*.

expansion fittings (transition fittings) to effect changes in tube diameter. The DEPOSITION code does not currently have the capability to either predict the aerosol particle losses in transition fittings or to account for turbulent diffusion effects on turbulent deposition in straight tubes.

The particle deposition in transition fittings (contraction and expansion fittings) has not received significant attention in the past. To date there are only limited data for the transition fittings and no simple correlations exist for predicting the aerosol particle losses in contraction or expansion fittings.

Particle deposition in straight tubes can be significant, particularly in situations where long sampling lines are required. One approach to minimize the losses in such situations is to employ large-diameter tubes and components (>25 mm) in the transport system. A sampling system using large diameter tubing has been used in the Swedish nuclear industry (Ström, 1989). In such a system, flow is drawn at a high flow rate from the stack through the large diameter transport tube to a location where a sub-sample is extracted for collection or analysis. Both the primary and secondary sampling flows are then returned to the stack. The DEPOSITION code can be used to demonstrate the benefit of using a large diameter transport tube system. Sample transport systems are illustrated in Figure 1.1, that use a conventional transport design (Figure 1.1a) and a large-diameter transport line design (Figure 1.1b). The collector or analyzer is assumed to have a 57 L/min (2-cfm) flow requirement. In the conventional sampling system, the flow is extracted at a rate of 57 L/min using a single probe and transported to the analysis or collection through a 28 mm diameter tubing system. The 28 mm diameter is selected

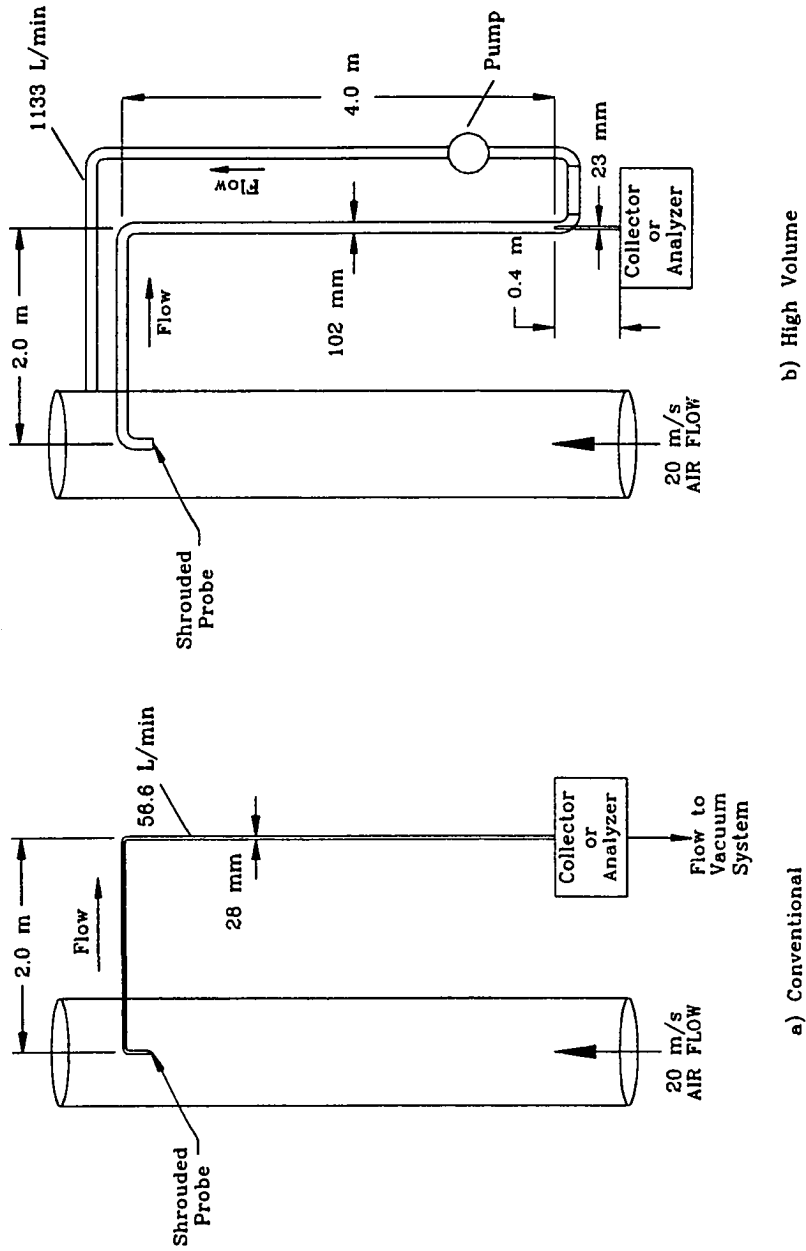


Figure 1.1. Comparison of conventional and large transport line sampling systems.

because it provides optimal penetration through the transport system for 10 μm aerodynamic diameter (AD) aerosol particles at the prescribe flow rate (predicted by the DEPOSITION code). In the large-diameter transport system (Figure 1.1b), the aerosol is transported at a flow rate of 1133 L/min (40-cfm) through a 102 mm (4-inch) diameter tube to the vicinity of the collector or analyzer. There, a 57 L/min sub-sample is extracted for collection or analysis. For 10 μm AD aerosol particles, the DEPOSITION code predicts a 72% transmission of the aerosol through the conventional system and a 90% transmission through the large-diameter transport tube system. Although this analysis shows the benefit of using a large-diameter transport, there is a limitation exists in the prediction capabilities of the DEPOSITION code, namely, the sub-model used to predict turbulent deposition is based on models that were either based on, or constrained by, data from tests with small tubes (~ 12 mm or 1/2-inch). This could be of significance when predicting the performance of large-diameter transport systems.

In the study presented herein, a set of experiments were conducted over a range of conditions as a means of generating a data base that was used to develop a correlation for predicting the aerosol particle loss in contraction and expansion fittings of arbitrary half-angles. In addition to the experimental work for the contraction fittings, the numerical methodology of Gong et al. (1993) was modified to numerically predict the particle losses in contraction fittings. Also within this study, tests were conducted over a broad range of conditions that allowed the determination of a Reynolds number effect on the aerosol particle deposition in vertical tubes. The data from the experiments was used to develop

a correlation that incorporates the Reynolds number to account for turbulent diffusion effects.

The organization of this dissertation is as follows: In Chapter II, a review of the literature available for the particle deposition in transition fittings and transport tubes is presented. In Chapter III, the numerical methodology used to model the losses in contraction fittings is discussed. In Chapter IV, the details of the experimental methodology used for testing the transition fittings and the large-diameter transport lines are presented. In Chapter V, the experimental and numerical results for contraction fittings are presented and discussed, and a correlation for predicting the aerosol losses in a contraction fitting is given. In Chapter VI, the results for the expansion fittings are presented and discussed; and, a correlation for predicting the aerosol losses in expansion fittings is also provided. In Chapter VII, the experimental results for the large-diameter transport lines are presented and discussed, and a correlation including the flow Reynolds number is given. Lastly, in Chapter VIII, a summary of this study is presented and conclusions are drawn.

CHAPTER II

LITERATURE SURVEY

Aerosol particle deposition in an abrupt contraction was studied in connection with the human respiratory system (Kim et al., 1984; and Itoh et al. 1985) and the modelling of filtration efficiency of membrane filters (Pich, 1964; Smutek and Pich, 1974; Smith and Phillips, 1975; Kanaoka et al., 1979; Ye and Pui, 1990; and Chen and Pui, 1995). Except for the study of Itoh et al. and Chen and Pui, the studies have been limited to laminar flow and contraction half-angle of 90°. The study of Chen and Pui includes the effect of contraction half-angle on aerosol deposition. To date there is no simple and accurate model to predict aerosol particle losses in contraction or expansion fittings when the flow is not laminar.

The modelling of aerosol losses in expansion fittings received limited attention in the past (Sommerfeld et al., 1992; Hardalupas et al., 1992; and Kindler et al., 1991); moreover, the studies have primarily focused on large particles ($D_p > 10 \mu\text{m}$) and are limited to expansion half-angles of 90° (Sommerfeld et al., 1992; and Hardalupas et al., 1992). Currently, there is no general model for predicting the aerosol losses in expansion fittings.

There has been a significant number of experimental and theoretical investigations on the aerosol particle deposition in turbulent duct flow (Friedlander and Johnstone, 1957; Postma and Schwendiman, 1960; Davies, C. N. 1966; Wells and Chamberlain, 1967; Sehmel, 1970; Farmer et al., 1970; Ilori, 1971; Fomey and Spielman, 1974; Liu and Agarwal, 1974; Cleaver and Yates, 1975; Onda, 1977; Papavergos and Hedley, 1984;

Fichman et al., 1988; and Fan and Ahmadi, 1993). Table 2.1 gives a summary of the experimental conditions for some of the studies on particle deposition in vertical tubes. Models generated from these studies are largely based on empiricism and show a correlation between a dimensionless deposition velocity and particle relaxation time. However, the supportive experiments have not been conducted with large-diameter tubes at high flow rates, so there is a lack of information upon which to determine if a Reynolds number effect should be included in the models.

The first useful theoretical model for aerosol particle deposition in turbulent gas flows in tubes was that of Friedlander and Johnstone (1957). Davies (1966), Beal (1970), and Liu and Ilori (1974) introduced modifications to improve the Friedlander and Johnstone theory while still retaining its basic concept, which is that of a free-flight stopping distance. More recently, Cleaver and Yates (1975), Papavergos and Hedley (1984), Fichman et al. (1988), and Fan and Ahmadi (1993) used a probabilistic theory approach to model the deposition phenomena in turbulent flows. These approaches are more realistic than the previous theories because they couple the deposition phenomena to the turbulent phenomena in the near-wall region.

Significant variations in relationships between the non-dimensional deposition velocity, V_+ , and the non-dimensional particle relaxation time, τ_+ , have been observed (e.g., Onda, 1977; and Papavergos and Hedley, 1984). The parameter v_+ is given by:

$$v_+ = \frac{V_d}{V_*} \quad (2.1)$$

where: V_d is the turbulent deposition velocity, which can be determined from experimental

TABLE 2.1. Previous Work on Particle Deposition in Vertical Tubes.

Particle Material	Friedlander and Johnstone (1957)	Postma and Schwendiman (1960)	Wells and Chamberlain (1967)	Sehmel (1970)	Farmer, Griffith, and Rhosenow (1970)	Ilori (1971)	Forney and Spielman (1974)	Liu and Agarwal (1974)
	Iron, Aluminum	ZnS, Glass	Tri-Cresyl Phosphate	Uranine, Uran. Meth. Blue	Water	Methylene and Uranine	Pollen, Spores, Polysty. sph.	Uranine and Olive Oil
Particle Size (μm)	.8-2.63 (polydisperse)	2,4,30	.15 - 5	2	93 - 262 (polydisperse)	9	19.5-48.5	1.4 - 21
Tube ID (cm)	.54, 1.3, 1.38	1.38-2.54	1.27, 3.81	.53 - 7.16	1.27	2.8	1.3 - 4.4	1.27
Re range	3×10^3 - 2.8×10^4	3×10^3 - 2×10^4	1×10^3 - 5.1×10^4	3×10^4 - 4×10^4	1.4×10^4 - 3×10^4	---	4×10^3 - 6×10^4	1×10^4 - 5×10^4
τ^+ range	0.74 - .1	0.1 - 10	7×10^{-4} - 2.4	1.2 - 10	3500 - 51000	0.3-200	22.5 - 715	0.21 - 770
V+ range	3×10^{-4} - 3×10^{-2}	6×10^{-6} - 4×10^{-2}	8×10^{-6} - 1×10^{-3}	3×10^{-5} - 1×10^{-2}	9×10^{-5} - 4×10^{-1}	6×10^{-3} - 0.1	8×10^{-2} - 0.5	6×10^{-5} - 0.15

data using the relationship :

$$V_d = \frac{Ud_t}{4L} \ln\left(\frac{1}{P}\right) \quad (2.2)$$

Here: U is the mean axial velocity in the tube; d_t is the tube diameter; L is the tube length; P is the aerosol particle penetration through the tube section. The parameter V_* , given in Equation 2.1 is the friction velocity, which is defined as:

$$V_* = U \sqrt{\frac{f}{8}} \quad (2.3)$$

where f is the Blasius friction factor for smooth tubes (Schlichting, 1979):

$$f = \frac{0.316}{Re^{1/4}} \quad (2.4)$$

Here Re is the flow Reynolds number based on the tube diameter (i.e., $Re = Ud/\nu$, where ν is the kinematic viscosity of the transport gas, which is normally air). The dimensionless relaxation time, τ_* , is defined as:

$$\tau_* = \frac{\tau V_*^2}{\nu} \quad (2.5)$$

where τ is the dimensional particle relaxation time. In turn, τ is given by:

$$\tau = \frac{C_c \rho_p D_p^2}{18\mu} \quad (2.6)$$

The symbol C_c represents the Cunningham slip correction factor (Fuchs, 1964); ρ_p represents the particle density; D_p represents the particle diameter; and, μ represents the

dynamic viscosity of air. The particle relaxation time represents the time required for the particle to adjust its velocity to a change in the force field affecting it.

Papavergos and Hedley (1984) suggest that the observed scatter in data correlating V_* as a function of τ_* may be due, in part, to a flow Reynolds number effect. Other factors that add uncertainty to the existing data base include the use of polydisperse, and possibly charged, aerosols in studies that were conducted before the current monodisperse aerosol generators and charge neutralization apparatus became available.

The particle deposition in turbulent flows in the region $0.1 \leq \tau_* \leq 100$ is primarily governed by particle inertia and turbulence effects. Other effects such as gravitational and electrostatic forces can be minimized by running the experiments with the tubes in a vertical orientation and by using a charge neutralizer. Any particle rebound or re-entrainment effects can be minimized by using liquid particles.

Some of the data scatter can be attributed to a turbulent diffusion effect that cannot be accounted for by τ_* alone, but can be taken into account as a Reynolds number effect. The diffusion of particles towards the wall is primarily due to the radial component of turbulence. Earlier researchers modelled this by assuming that the particle diffusivity was equal to, or a function of, the fluid momentum diffusivity (Friedlander and Johnstone, 1957; Davies, 1965; Beal, 1970; and Liu and Ileri, 1974). Tennekes and Lumley (1992) have shown that turbulent diffusion is a function of Reynolds number. To characterize the radial turbulent diffusion, the Reynolds number should be defined based on the r.m.s. value of the radial velocity fluctuation, v' and the tube diameter. Laufer (1953) showed that v'/V_* was nearly constant in the core region so by the definition of V_* given in Equation 2.3, it can

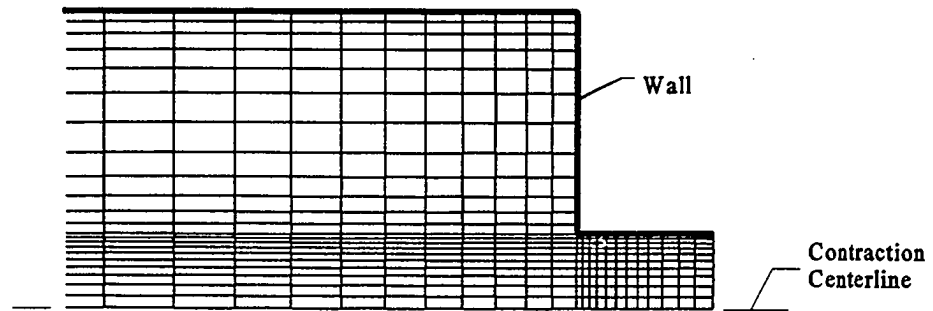
be seen that the r.m.s value of the radial velocity fluctuations can be characterized by the tube mean velocity, U . Hence, the Reynolds number based on the duct mean velocity and tube diameter can be used to account for turbulent diffusion effects not captured by the non-dimensional particle relaxation time.

CHAPTER III

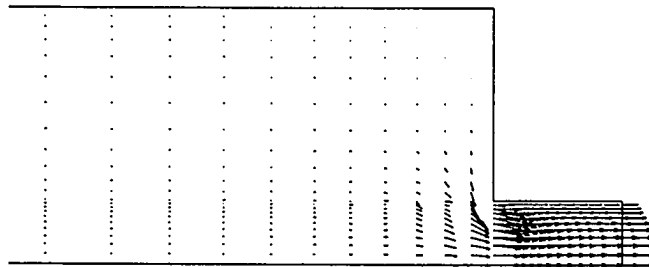
NUMERICAL PROCEDURE

A numerical approach that includes the effects of turbulence was used to examine the wall loss in contraction fittings. The numerical predictions of the particle losses were performed following a model developed by Gong et al. (1993). The assumptions for the analysis are as follows: 1) The concentration of particles in the gas phase is very low (volume ratio $\sim 10^{-10}$); therefore, the particles do not affect the gas flow and the particle-particle interactions are negligible. The gas-particle interaction is assumed to be one way. 2) The mean flow is steady, incompressible, isothermal, and axi-symmetric. 3) Turbulence is isotropic.

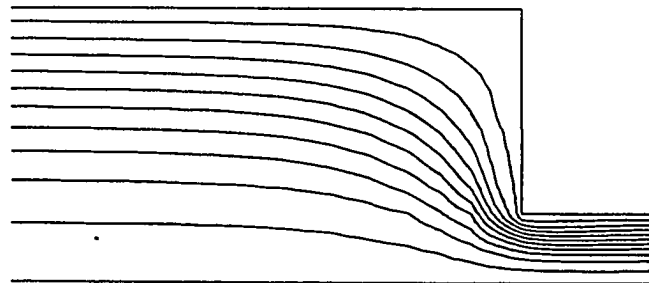
The gas flow in a tube with a 90°, 45°, and 12° contraction fittings for area ratios of 1.78, 4 and 16 were modeled using FIDAP (1993), a commercially available finite element flow solver. An axi-symmetric grid with four node quadrilateral elements was used to generate the geometrical mesh for the solver and a standard κ - ϵ model was used to model turbulence. An eight diameter entrance region was included in the flow domain to match the experimental setup. Computations were made on two different mesh sizes to show grid independence. Figure 3.1 shows a sample mesh, velocity vector field, and streamline distribution for a contraction fitting with a 90° half-angle. The turbulence intensity at the inlet of the tube was set to 3.5% for the analyses; however, halving or doubling this value did not have a significant influence on the aerosol particle losses in the contraction.



a) Computational mesh.



b) Velocity Vectors.



c) Streamlines.

Figure 3.1. Sample computational mesh, velocity vectors, and streamlines for a contraction fitting.

The particle trajectories were predicted using a Lagrangian approach. The equations of motion governing the particle trajectory are:

$$\frac{du_p}{dt} = \frac{3}{4} \frac{\rho}{\rho_p D_p} C_D (u - u_p) |U - U_p| + g + f_{Lz} \quad (3.1)$$

$$\frac{dv_p}{dt} = \frac{3}{4} \frac{\rho}{\rho_p D_p} C_D (v - v_p) |U - U_p| + \frac{w_p^2}{r_p} + f_{Lr} \quad (3.2)$$

$$\frac{dw_p}{dt} = \frac{3}{4} \frac{\rho}{\rho_p D_p} C_D (w - w_p) |U - U_p| - \frac{w_p v_p}{r_p} \quad (3.3)$$

where U and U_p are the instantaneous gas and particle velocities, respectively. The parameter ρ is the gas density, C_D is the particle drag coefficient; v , w , and u are the radial, tangential, and axial gas velocities respectively; and v_p , w_p , and u_p are the particle velocity components. The terms f_{Lr} and f_{Lz} are the Saffman force per unit mass in the radial and axial directions, respectively.

It is important to note that the fluid velocity, U , is the sum of the average gas velocity and a fluctuating component:

$$U = \bar{u} + u' \quad (3.4)$$

where \bar{u} is the average fluid velocity (obtained from FIDAP) and u' is the random fluctuating component (obtained from the methodology described in Gong et al. (1993)). Equations 3.1-3.3 are numerically integrated to obtain the particle velocity (v_p , w_p , u_p) and

the particle trajectory (r_p, θ_p, z_p) is evaluated by numerically integrating the following equations:

$$\frac{dr_p}{dt} = v_p \quad (3.5)$$

$$\frac{d\theta_p}{dt} = \frac{w_p}{r_p} \quad (3.6)$$

$$\frac{dz_p}{dt} = u_p \quad (3.7)$$

where r_p , θ_p , and z_p are the radial, tangential, and axial particle displacements; respectively. The losses in the contraction fittings were computed by tracking the particle trajectories of several thousand particles. Once a particle strikes a wall, the particle is assumed to adhere to the wall (i.e. an attachment coefficient of unity). By counting the number of particles deposited on the wall of a contraction fitting, a wall loss ratio can be determined.

Prior to performing extensive analyses on the contraction fittings, a grid independence study was carried out to establish the mesh size to be used in the analyses. Two mesh sizes were considered for the three contraction angles. It was found that increasing the initial mesh size by a factor of 1.6 caused less than 1 percent change in the mass flow rate through the fitting, indicating the solution was grid independent using these mesh sizes. Table 3.1 shows the results of the grid independence study. The larger mesh

TABLE 3.1. Grid Independence Study.

Contraction Half-Angle					
90°		45°		12°	
No. of Points	Mass Flow	No. of Points	Mass Flow	No. of Points	Mass Flow
983	.767	975	.771	1275	.768
618	.760	605	.766	744	.766

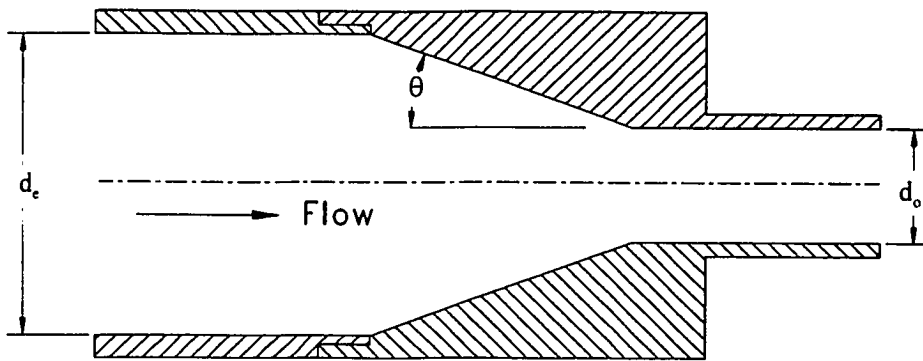
size was used for all analyses. The number of particles tracked was established by successively increasing the number of particles until consecutive results of wall loss ratio did not vary more than 3%. Similarly, the time step was established by successively decreasing it until less than 3% change observed between consecutive results.

CHAPTER IV

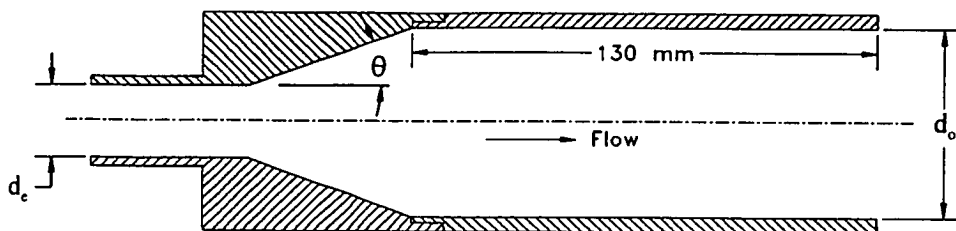
EXPERIMENTAL PROCEDURES

Figure 4.1a is a schematic of a contraction fitting and Figure 4.1b is a schematic of an expansion fitting. In the figures, d_e is the entrance diameter, d_o is the outlet diameter, and θ is the contraction or expansion half-angle. The apparatus used to test the contraction fittings, expansion fittings, and large transport tubes is shown in Figures 4.2-4.4; respectively. For the contraction study, half-angles of 12° , 45° , and 90° were used to transition a 27 mm diameter tube to either a 13 mm or a 6.7 mm diameter tube. A 45° and a 90° half-angle were also used to transition a 52 mm diameter tube to a 13 mm diameter. For the expansion fitting study, half-angles of 3° , 6° , 12° , 45° , and 90° were used to transition a 6.7 mm and 13 mm diameter tube to a 27 mm diameter tube. In addition, a 21 mm diameter tube was transition to a 27 mm diameter tube using 3° , 12° and 90° half-angles. A 130 mm straight tube extension was added at the end of all expansions to capture downstream effects caused by the expansion. Four tubes were used in the large transport line study: 102 mm diameter by 5.5 m long, 52 mm diameter by 2.7 m long, 26 mm diameter by 2.7 m long, and a 13 mm diameter and 2.7 m long. Detailed dimensions for the contraction/expansion fittings are given in Appendix D.

In all the studies, a vibrating jet atomizer (Berglund and Liu, 1973) was used to generate a nearly monodisperse aerosol from a mixture of oleic acid, alcohol, and sodium fluorescein (analytical tracer). The generated aerosol was passed by a 10 mCi Kr-85 source to neutralize electrical charge. The aerosol particle mean diameter was determined by



a) Contraction fitting



b) Expansion fitting

Figure 4.1. Schematic of transition fittings.

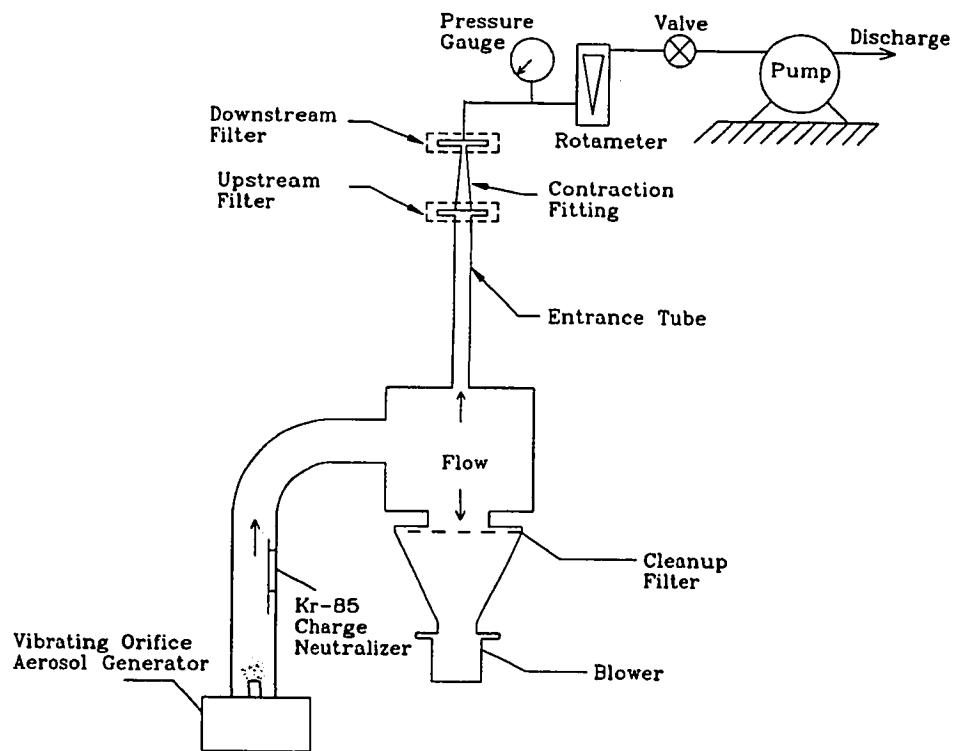


Figure 4.2. Experimental setup for testing contraction fittings.

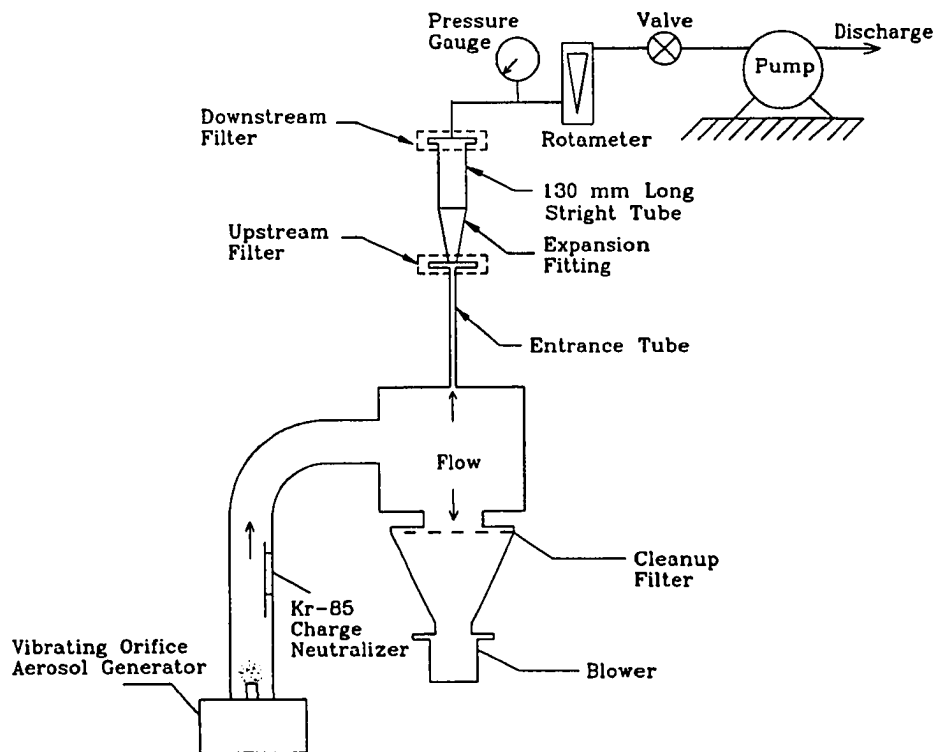


Figure 4.3. Experimental setup for testing expansion fittings.

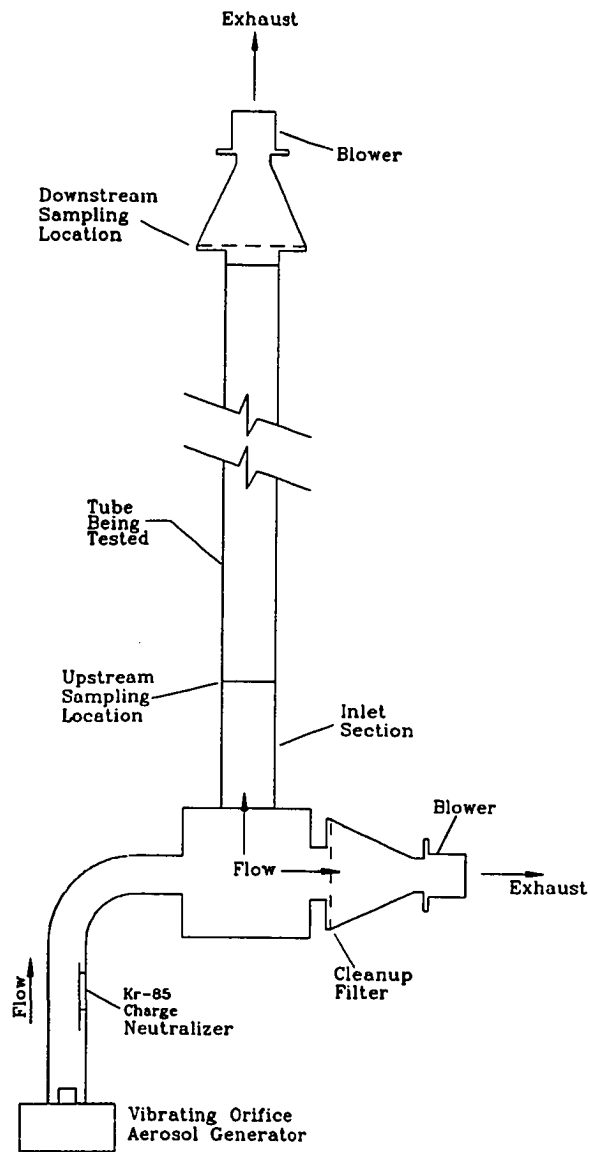


Figure 4.4. Experimental setup for testing large transport tubes.

collecting a sample on an oil-phobic glass slide and then measuring the apparent sizes under a microscope. To account for gravitational flattening, the observed mean diameter was corrected by a factor, f_f , developed by Olan-Figueroa et al. (1982). The mean aerodynamic diameter, D_a of the aerosol particles was calculated from :

$$\sqrt{\rho_w C_a} D_a = \sqrt{\rho_p C_p} D_p \quad (4.1)$$

where: ρ_w is the density of water, C_a is the Cunningham correction based on the aerodynamic diameter; D_p is the particle diameter; ρ_p is the particle density (0.933 g/cm³ for mixture of sodium fluorescein and oleic acid); and C_p is the Cunningham correction factor based on the particle diameter. A flattening factor of 1.32 was used for the mixture employed in these experiments. The aerodynamic particle diameters used in the tests ranged from 5 to 20 μm .

The electrically neutralized aerosol was drawn into a plenum chamber where the flow was split. A portion of the flow was diverted into the vertically-oriented test section while the remaining excess flow was drawn through a cleanup filter and the air was exhausted from the system. To minimize entrance effects, the test flow was drawn into a straight tube that was at least eight diameters in length. A filter sample was first collected at the exit of this section (upstream filter in Figures 4.2-4.4), then the test section (contraction fitting, expansion fitting, or transport tube) was inserted into the flow circuit and a filter sample was collected at its exit plane (downstream filter). This process of collecting filter samples upstream and downstream of the contraction fitting being tested was repeated at least four times for each set of test conditions.

Sodium fluorescein was eluted from the sampling filters with a mixture of isopropyl alcohol and water. Three fluorometer readings were taken on aliquots of each filter solution using a Sequoia-Turner Model 450 fluorometer (Sequoia-Turner Corp., Mountain View, CA). Aerosol penetration through the contraction fitting, P , was calculated from:

$$P = \frac{c_{dn}}{c_{up}} \quad (4.2)$$

Here: c_{dn} is aerosol concentration at the exit plane of the test section; and, c_{up} is the aerosol concentration at the exit of the inlet section (no test section in place). The concentration values were based on fluorometer readings, sampling time, volume of fluid used to elute tracer, and flow rate through the system.

The wall loss, WL , is used as the dependent variable in presenting the results for the contraction and expansion fitting studies. The wall loss was calculated from:

$$WL = 1 - P. \quad (4.3)$$

Davies (1966) noted that flow swirl in transport tubes would cause particles to experience a centrifugal force, which could cause them to deposit on the walls at a higher rate than would occur for pure turbulent deposition. The flows in the 102, 52, and 26 mm tubes were checked for swirl at flow rates 453 and 1730 L/min. A three-port directional pitot probe was inserted into the tube and the probe was rotated such that the pressures at the two outboard ports were balanced. The angle associated with the balanced condition was measured. For all conditions, the pressures balanced at zero degrees (flow perpendicular to the probe), indicating there was no flow swirl. Swirl in the 13 mm tube was not tested due to size restrictions in using the directional probe.

CHAPTER V

CONTRACTION FITTINGS

Ye and Pui (1990) observed that the aerosol particle losses in a contraction are a function of the contraction area ratio, A_o/A_e , and the Stokes number, Stk_c ; where Stk_c is defined as:

$$Stk_c = \frac{\rho_p D_p^2 C_p U_e}{9\mu d_o} \quad (5.1)$$

where: U_e is the entrance velocity and μ is the viscosity of air. Ye and Pui also found that the losses in the contraction were independent of the flow Reynolds number and that the losses correlate with the parameter $Stk_c^{0.5}/(d_o/d_e)^{0.31}$.

In contrast with the results of Ye and Pui, in this study, the results are that for a constant contraction angle, the wall losses correlated best with the parameter $Stk_c(1-A_o/A_e)$. Plots of the wall loss as a function of $Stk_c(1-A_o/A_e)$ for contraction half-angles of 12°, 45°, and 90° are given in Figures 5.1, 5.2, and 5.3; respectively. Error bars on the data points represent a 95% confidence interval about the mean of replicate experiments for a given set of conditions. The uncertainties range from 1.5% and 15.9% for the 12° contraction fitting, from 1.3% to 15.0% for the 45° contraction fittings, and 1.1% to 14.2% for the 90° contraction fitting. The uncertainties were calculated as prescribed by ANSI/ASME PTC 19.1-1985 (1985). Appendix B contains the details of the uncertainty

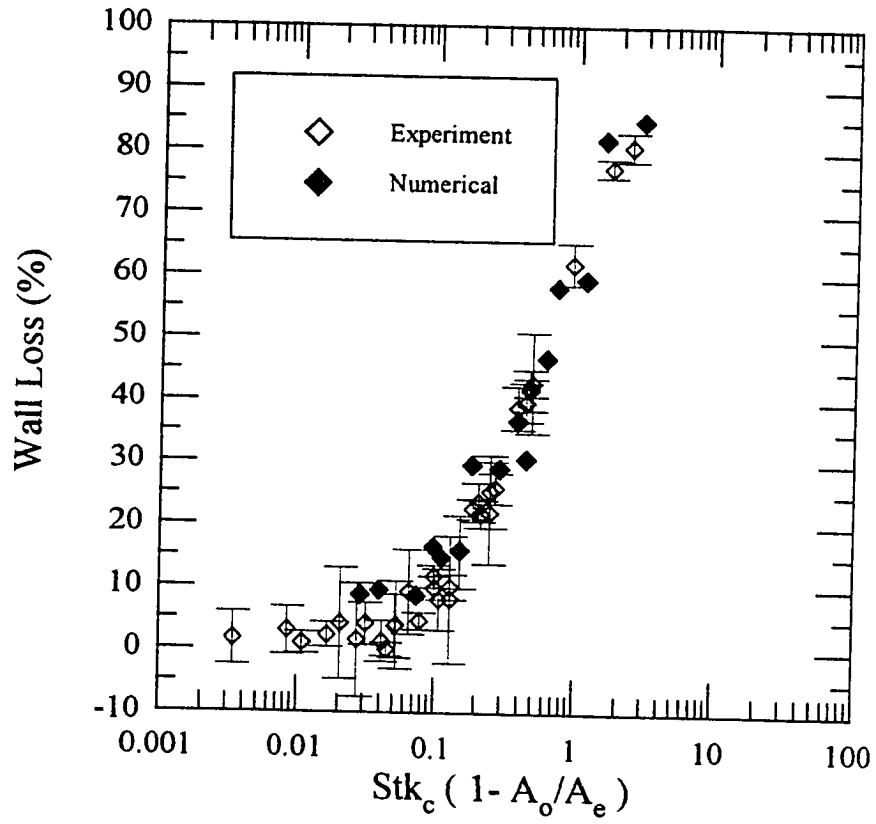


Figure 5.1. Wall loss for 90° contraction fittings.

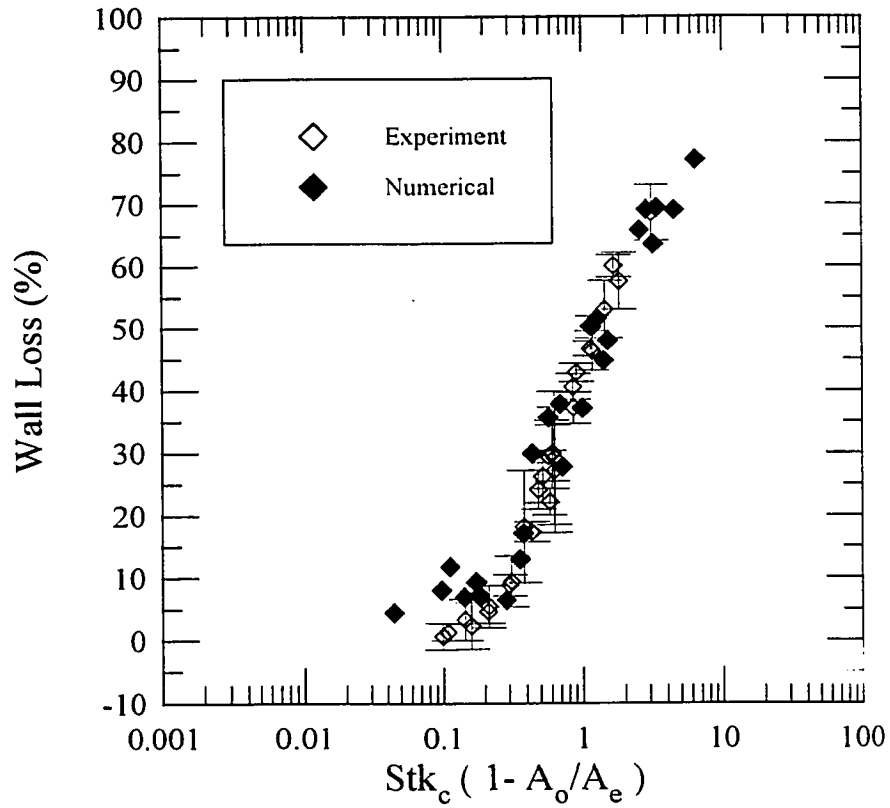


Figure 5.2. Wall loss for 45° contraction fittings.

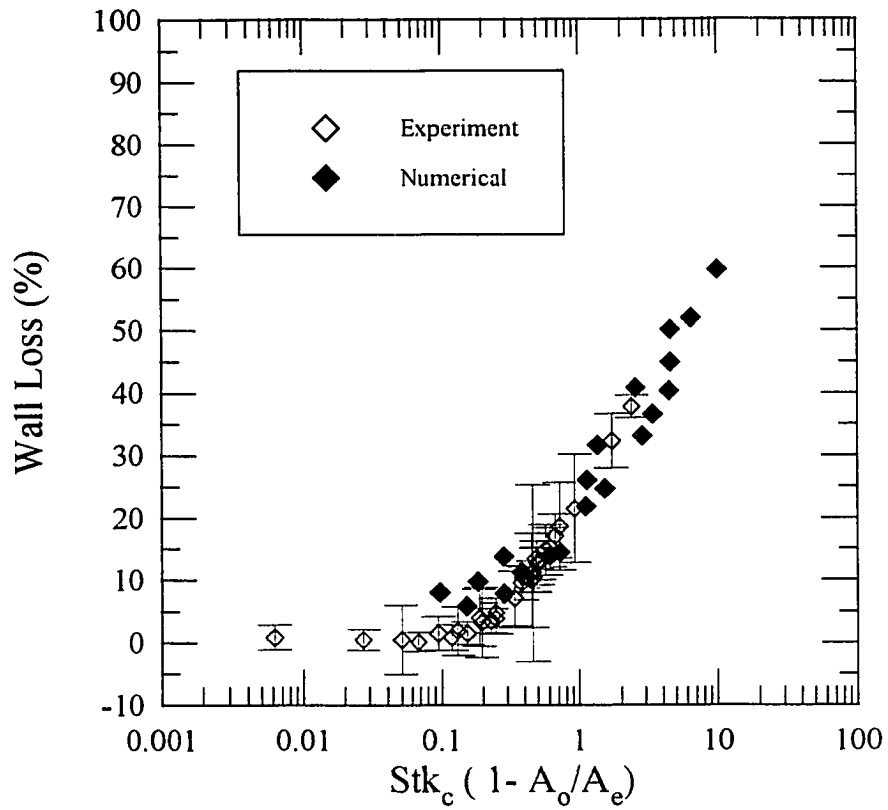


Figure 5.3. Wall loss for 12° contraction fittings.

calculations. The data for the contraction fittings are presented in tabular form in Appendix C.

The numerically predicted values of wall loss are included in Figures 5.1 through 5.3. As may be noted, the numerically predicted wall loss values are in good agreement with the experimental data. The numerical data are presented in tabular form in Appendix D.

The experimentally determined wall loss data for the contraction fittings in Figures 5.1-5.3 were correlated using an equation of the form:

$$Wl = \frac{1}{1 + \left(\frac{X}{a_1 e^{a_2 \theta}} \right)^{a_3}} \quad (5.2)$$

where X is the parameter $Stk_c (1 - A_o/A_c)$, θ is the contraction half-angle in degrees, and a_1 , a_2 , and a_3 are constants determined by a least squares procedure. Other equations were evaluated; however, Equation 5.2 produced the best fit to the data. The values of the coefficients obtained from the least squares procedure were:

$$\begin{aligned} a_1 &= 3.1393 \\ a_2 &= -0.01849 \\ a_3 &= -1.2439 \end{aligned}$$

Equation 5.2, with these coefficients, has a correlation coefficient, r^2 , to the experimental data of 0.987. It is noted that as the Stokes number becomes very large, the aerosol particles will travel in a straight line without being influenced by the contraction. For this upper limit, the aerosol particle deposition in contraction fittings will be equal to:

$$Wl = \left(1 - \frac{A_o}{A_e}\right) \quad (5.3)$$

Thus, Equation 5.2 is only valid up to the limiting value of $Wl = (1 - A_o/A_e)$.

Equation 5.2 represents a three dimensional surface, which is plotted in Figure 5.4 with the experimental data superimposed on it. The surface covers the range of independent variables of $0.001 \leq Stk_c (1 - A_o/A_e) \leq 100$ and $12^\circ \leq \theta \leq 90^\circ$.

Given the geometry of the contraction fitting, the flow rate, and the aerodynamic particle diameter, Equation 5.2 can be used to determine the aerosol particle losses in a contraction fitting. Figure 5.5 is a plot of the wall loss for a 90° contraction fitting as predicted by Equation 5.2. Also included in the plot are the losses predicted by the correlation of Pich (1964), Ye and Pui (1990), and Chen and Pui (1995). Although correlations of these researchers are based on numerical studies for laminar flow they were chosen for comparison because they are the only available models.

The laminar model of Pich is of the form:

$$Wl = \frac{2Z}{1+G} - \frac{Z^2}{(1+G)^2} \quad (5.4)$$

where:

$$Z = 2A + 2A^2 \left[e^{\left(-\frac{1}{A}\right)} - 1 \right]$$

$$A = 4Stk\sqrt{G}$$

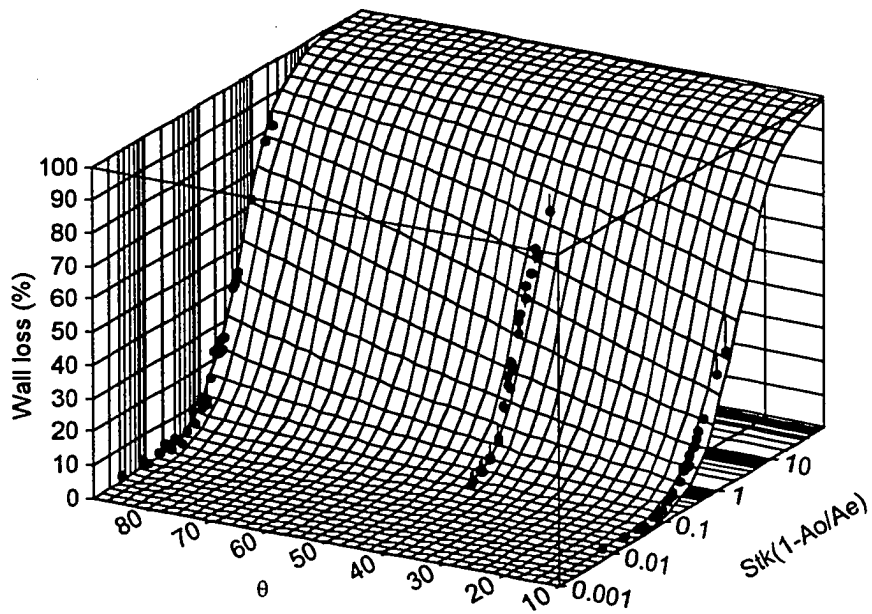


Figure 5.4. Correlation surface for contraction fittings.

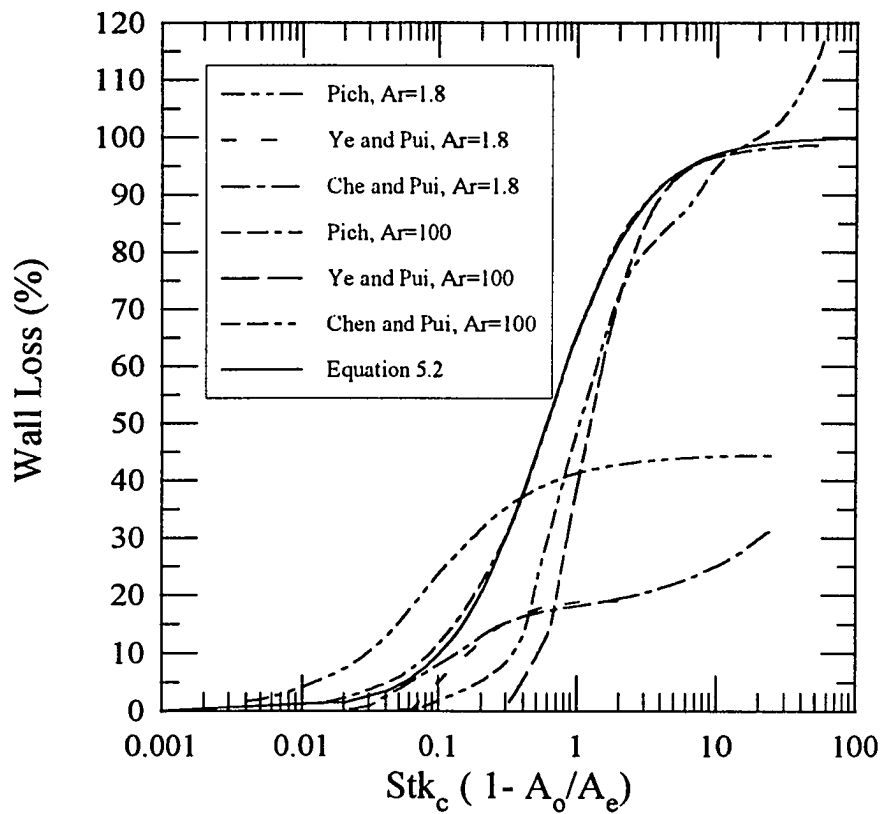


Figure 5.5. Comparison of aerosol particle losses for a 90° contraction fitting predicted by Equation 5.2 and the model of Pich (1964), Ye and Pui (1990), and Chen and Pui (1995).

$$G = \frac{\sqrt{\frac{A_o}{A_e}}}{\left[1 - \sqrt{\frac{A_o}{A_e}}\right]}$$

The correlation of Ye and Pui is of the form:

$$Wl = \left(1 - \frac{A_o}{A_e}\right) \left[1 - e^{(1.721 - 8.557S + 2.227S^2)}\right] \quad (5.5)$$

where S is defined as $Stk_c^{0.5}/(d_o/d_e)^{0.31}$. Chen and Pui present the following correlation for a contraction of arbitrary half-angle:

$$Wl = \left[0.882 + 0.0272y^{0.5} - 8.272y^{0.5} e^{(-3.627y^{0.5})^2}\right]^2 \left[1 - \frac{A_o}{A_e}\right]^2 \quad (5.6)$$

where:

$$y = \frac{Stk \sin(\theta)^{1.119}}{0.235 \left[\frac{A_e}{A_o}\right]^{0.305}}$$

The models of Ye and Pui and Chen and Pui were derived from numerical simulations of laminar flow in contraction fittings. Note that all the laminar models predict different loss characteristics for the contraction depending on the area ratio when the losses are plotted as a function of the parameter $Stk_c (1 - A_o/A_e)$. This phenomena; however, was not observed in the experimental data or numerical predictions. As an example, at a value of $Stk_c (1 - A_o/A_e)$ of 0.2 and expansion angle of 90°, the model of Pich, which is appropriate

only to a 90° angle, predicts the losses to be approximately 31.5% for an area ratio of 1.8 and 21.1% for an area ratio of 100. The model of Ye and Pui predicts the losses to be approximately 17.2% for an area ratio of 1.8 and 0% for an area ratio of 100. The model of Chen and Pui predicts 13.0% for an area ratio of 1.8 and 3.1% for an area ratio of 100. In contrast, the measured losses are approximately 22.6% and our model predicts 20.5% independent of area ratio. The model of Pich matches our model very well at values of area ratio greater than 20. At high area ratios, the other two models tend to underestimate the losses, particularly in the region of $Stk_c (1-A_o/A_e) < 1$. Figures 5.6 and 5.7 show a comparison of our model to the that of Chen and Pui at contraction half-angles of 45° and 12°, respectively. The model of Chen and Pui predicts different values of wall loss for different area ratios. At low values of $Stk_c (1-A_o/A_e)$, the model will predict the losses to be greater than 0% as can be seen from Figure 5.6. At high values of $Stk_c (1-A_o/A_e)$, the model predicts losses greater than 100% as seen in Figures 5.5 and 5.7 and does not follow the asymptotic behavior as shown by the model of Pich.

The losses in the contraction fittings are primarily due to inertial impaction. For a fixed contraction half-angle, the losses in the contraction fitting correlate very well with the parameter $Stk_c (1-A_o/A_e)$. For values of $Stk_c (1-A_o/A_e) < 0.2$ at $\theta = 12^\circ$; $Stk_c (1-A_o/A_e) < 0.15$ at $\theta = 45^\circ$; and, $Stk_c (1-A_o/A_e) < 0.05$ at $\theta = 90^\circ$ the losses in the contraction fitting are less than 5% and could be considered negligible. However, above these values of $Stk_c (1-A_o/A_e)$, the losses increase rapidly and should not be neglected. The aerosol particle losses for a given area ratio, particle size, and flow rate increase with

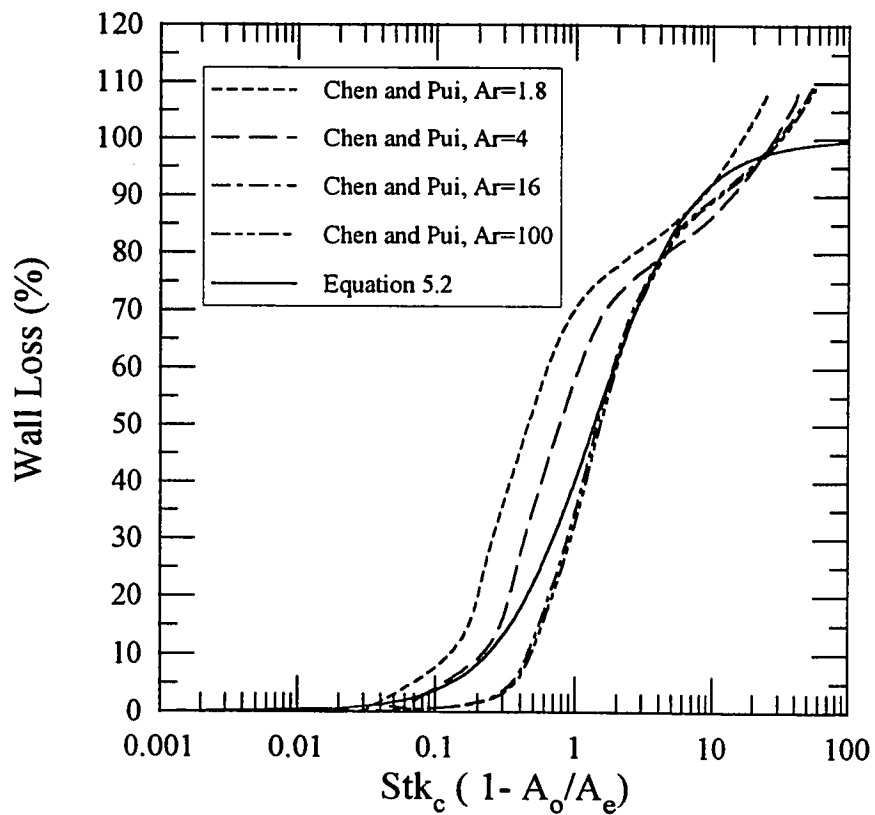


Figure 5.6. Comparison of aerosol particle losses for a 45° contraction fitting predicted by Equation 5.2 and the model of Chen and Pui (1995).

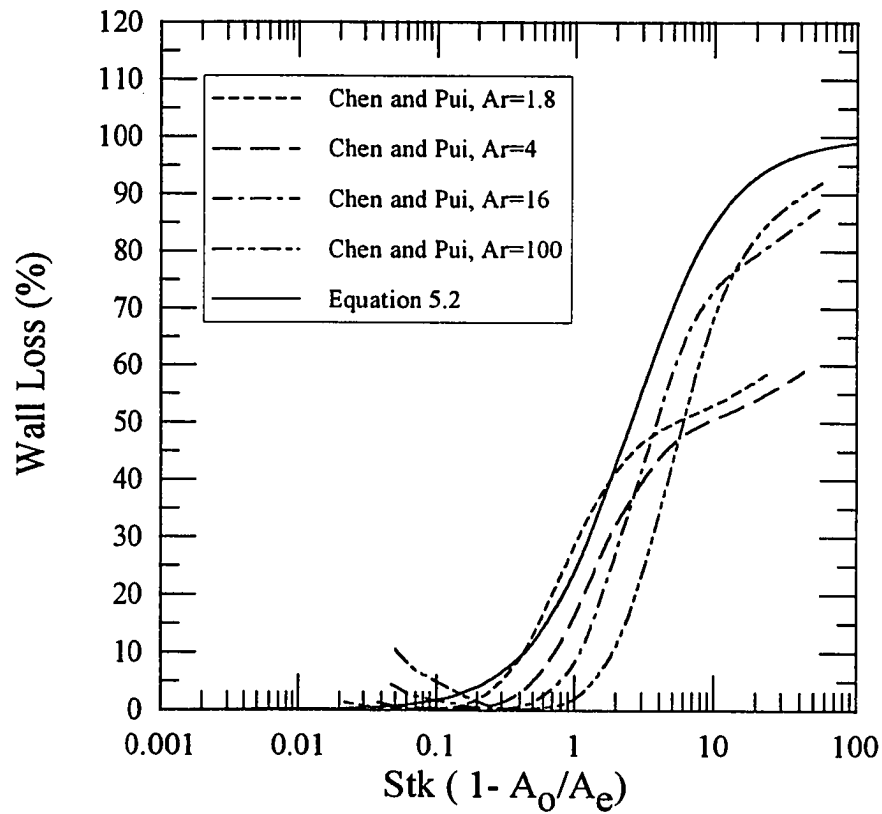


Figure 5.7. Comparison of aerosol particle losses for a 12° contraction fitting predicted by Equation 5.2 and the model of Chen and Pui (1995).

increasing contraction half-angle. Also, in general, the wall loss increases with increasing $Stk_c (1-A_o/A_e)$. This can be attributed to two effects: first; as Stk_c increases, the inertia of the particles increases causing the path of more particles to deviate from the fluid streamlines and strike the wall as the particles try to negotiate the air stream turn caused by the contraction. Second, as A_o/A_e decreases, the streamline curvature in the contraction region will become sharper causing more particles to strike the wall as they try to negotiate the turn in the air stream.

The numerical model used in this study shows good agreement with the experimental results; however, the numerical results show slightly more scatter than the experimental data. This can be partly attributed to the randomness built into the numerical procedure and the assumption that turbulence is isotropic. The numerical procedure involves the use of a Gaussian random number for generating the turbulent fluid velocity fluctuations; as a consequence, consecutive runs of the numerical procedure for the same contraction geometry, particle size and flow conditions will produce random variations (on the order of $\pm 2\%$) in the predicted values of wall loss. The numerical predictions show a maximum difference of approximately 11% for all contraction angles when compared to the experimental data. As should be expected, the inclusion of turbulence significantly improves the prediction accuracy when compared to the laminar model of Ye and Pui. The agreement of the experimental and numerical results suggests that losses of aerosol particles in contraction fittings could be determined numerically for conditions that are outside those for which the correlation applies, e. g., a fitting with contoured internal surfaces rather than straight lines.

CHAPTER VI

EXPANSION FITTINGS

Aerosol particle losses in a expansion fitting were found to be a strong function of the contraction area ratio, A_o/A_e , the expansion half-angle, θ , and the Stokes number, Stk_e ; where Stk_e is defined as:

$$Stk_e = \frac{\rho_p D_p^2 C_p U_o}{9\mu d_e} \quad (6.1)$$

Here: U_o is the outlet velocity.

Plots of the wall loss as a function of Stk_e for expansion half-angles of 3°, 6°, 12°, 45°, and 90° are given in Figures 6.1 through 6.5. Error bars on the data points represent a 95% confidence interval about the mean of replicate experiments for a given set of conditions. The uncertainties ranged from 1.5% to 22.2% for the 3° expansion fitting, from 1.3% to 33.6% for the 6° expansion fittings, from 1.8% to 19.9% for the 12° expansion fittings, from 2.2% to 18.7% for the 45° expansion fittings, and from 1.7% to 17.6% for the 90° expansion fittings. Details of the uncertainty calculation are presented in Appendix B. The experimentally determined wall loss data for the expansion fittings presented in Figures 6.1-6.5 were correlated using an equation of the form:

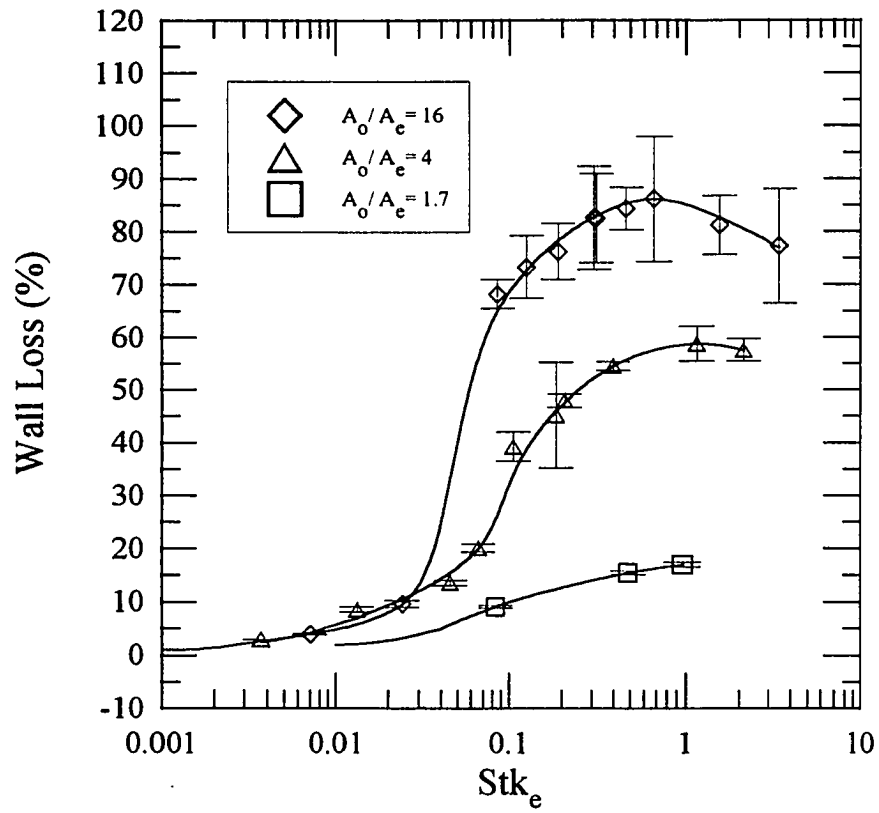


Figure 6.1. Wall loss for 3^0 expansion fittings.

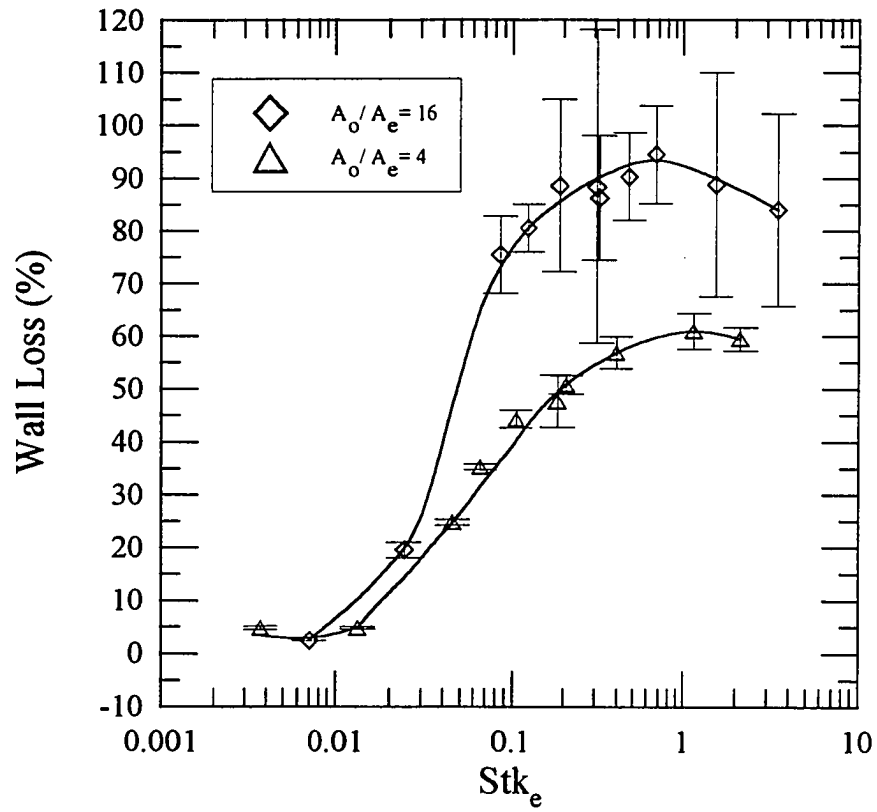


Figure 6.2. Wall loss for 6° expansion fittings.

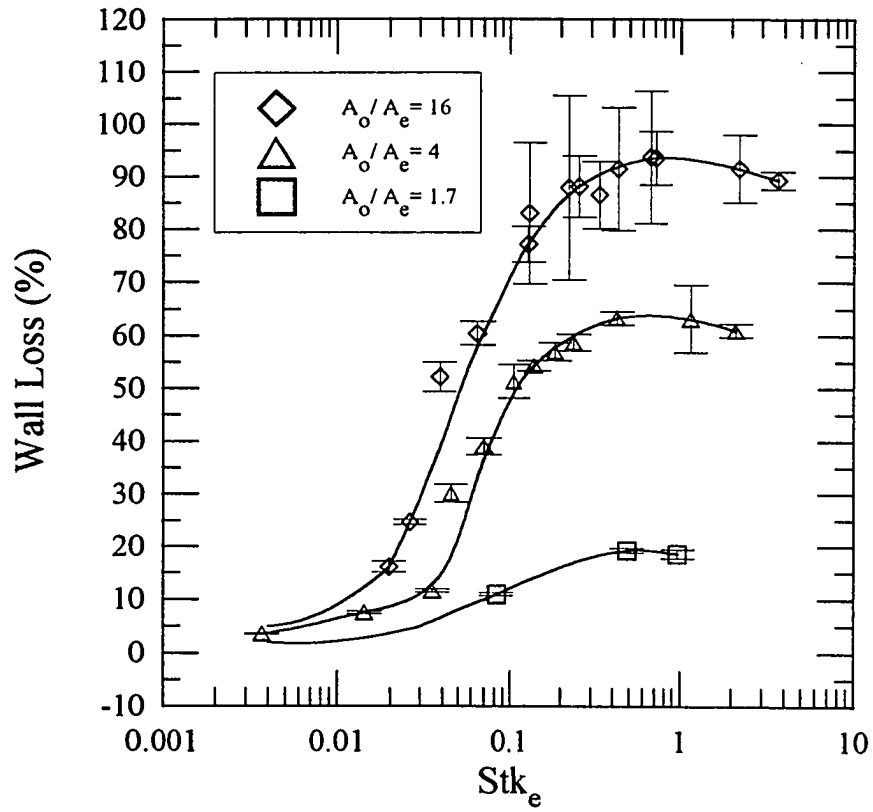


Figure 6.3. Wall loss for 12° expansion fittings.

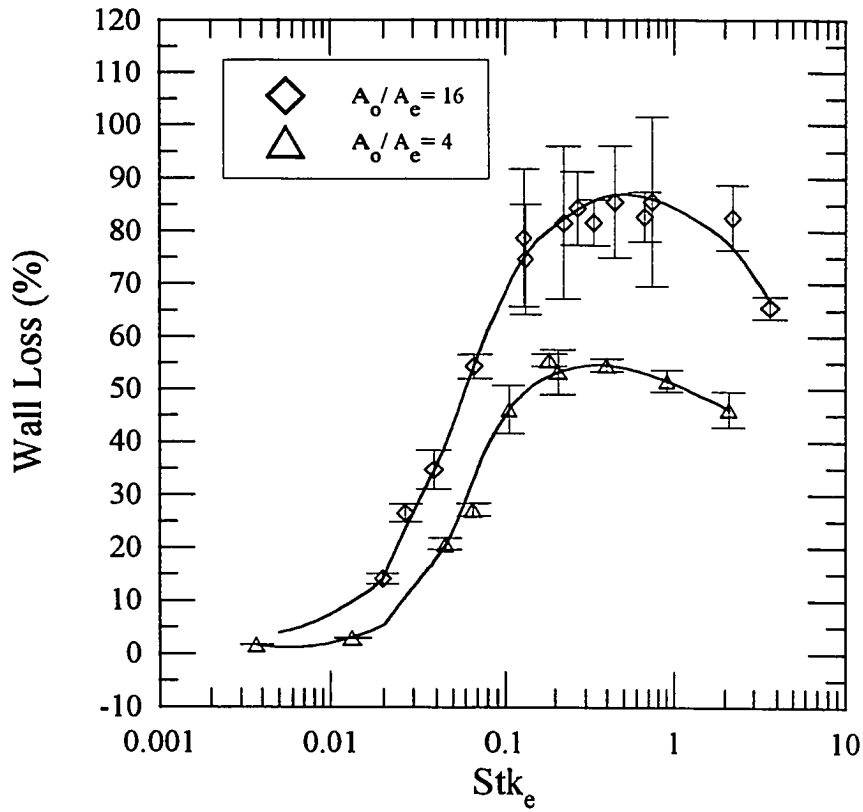


Figure 6.4. Wall loss for 45° expansion fittings.

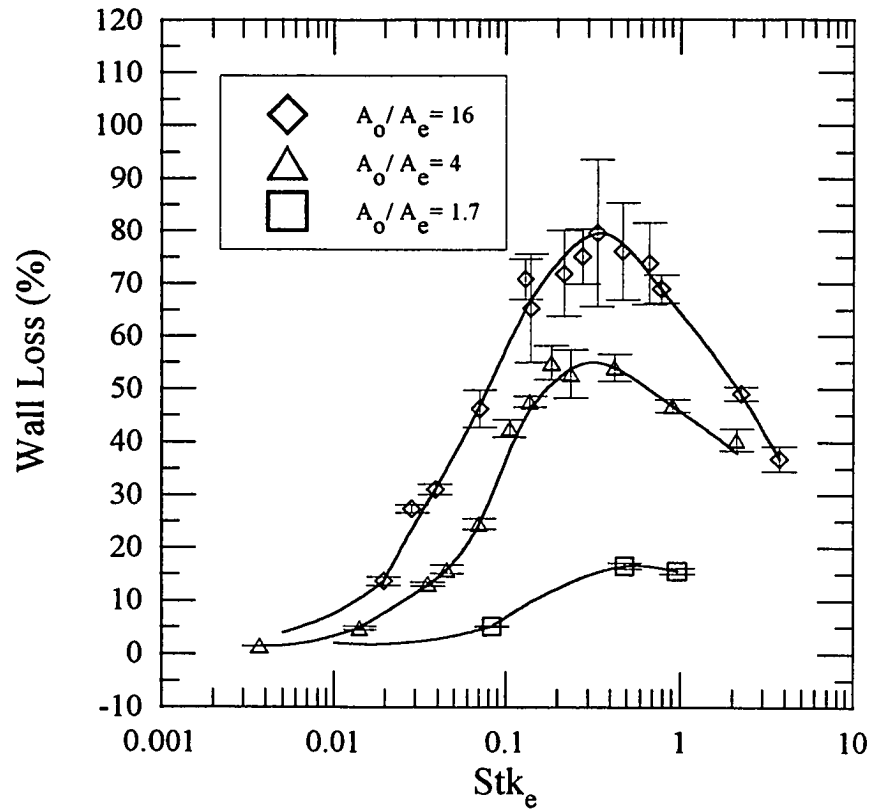


Figure 6.5. Wall loss for 90° expansion fittings.

$$WL = b_1 R^2 e^{-0.5 \left[\left(\frac{\ln \left(\frac{Stk_c R}{b_2} \right)}{b_3} \right)^2 + \left(\frac{\ln \left(\frac{\theta}{b_4} \right)}{b_5} \right)^2 \right]} \quad (6.2)$$

where R is the parameter $(1-A/A_o)$, θ is the expansion half-angle in degrees, and b_1 , b_2 , b_3 , b_4 and b_5 are constants determined by a least squares procedure. Other equations were evaluated; however, Equation 6.2 produced the best fit to the data. The values of the coefficients obtained from the least squares procedure where:

$$\begin{aligned} b_1 &= 1.1358 \\ b_2 &= 0.5518 \\ b_3 &= 1.9661 \\ b_4 &= 12.519 \\ b_5 &= 2.7825 \end{aligned}$$

Equation 6.2 has a correlation coefficient, r^2 , to the experimental data of 0.960 and covers the range of independent variables of $0.001 \leq Stk_c \leq 10$, $3^\circ \leq \theta \leq 90^\circ$, and $1.7 \leq A_o/A_e \leq 16$.

Figures 6.6-6.8 are plots of the wall loss for expansion fittings as a function Stk_c for various expansion half-angles at a fixed area ratio, which were generated using Equation 6.2. Based on these Figures and Figures 6.1-6.5, the following observations can be made about the aerosol losses in an expansion fitting:

Aerosol losses in an expansion fitting decrease with decreasing area ratio and losses are lowest for a 90° expansion half-angle and increase with decreasing half-angle down to a half-angle of approximately 12° ; thereafter, the losses decrease with decreasing half-angle. Losses are a maximum for a half-angle of approximately 12° . As the air flows into the

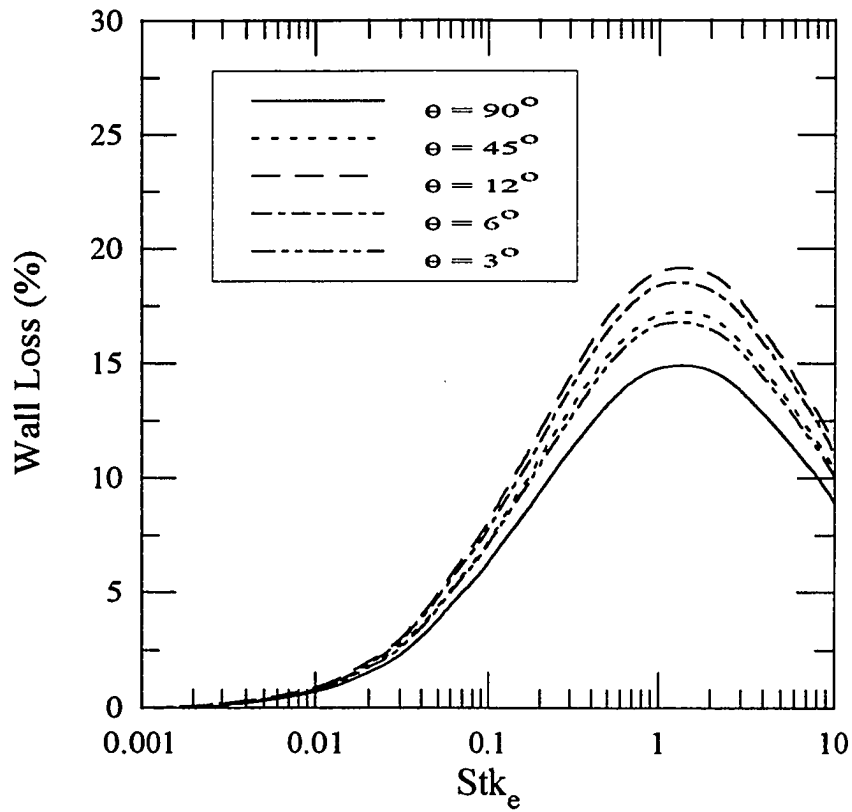


Figure 6.6. Wall loss for expansion fittings as predicted by Equation 6.2, $A_o/A_e = 1.7$.

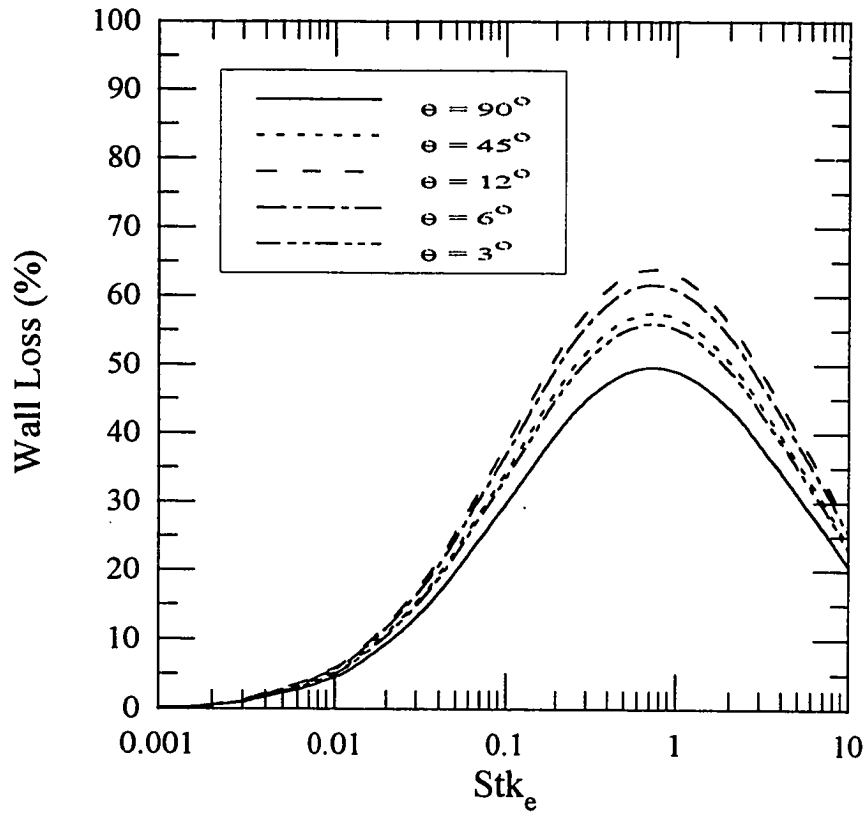


Figure 6.7. Wall loss for expansion fittings as predicted by Equation 6.2, $A_o/A_e = 4$.

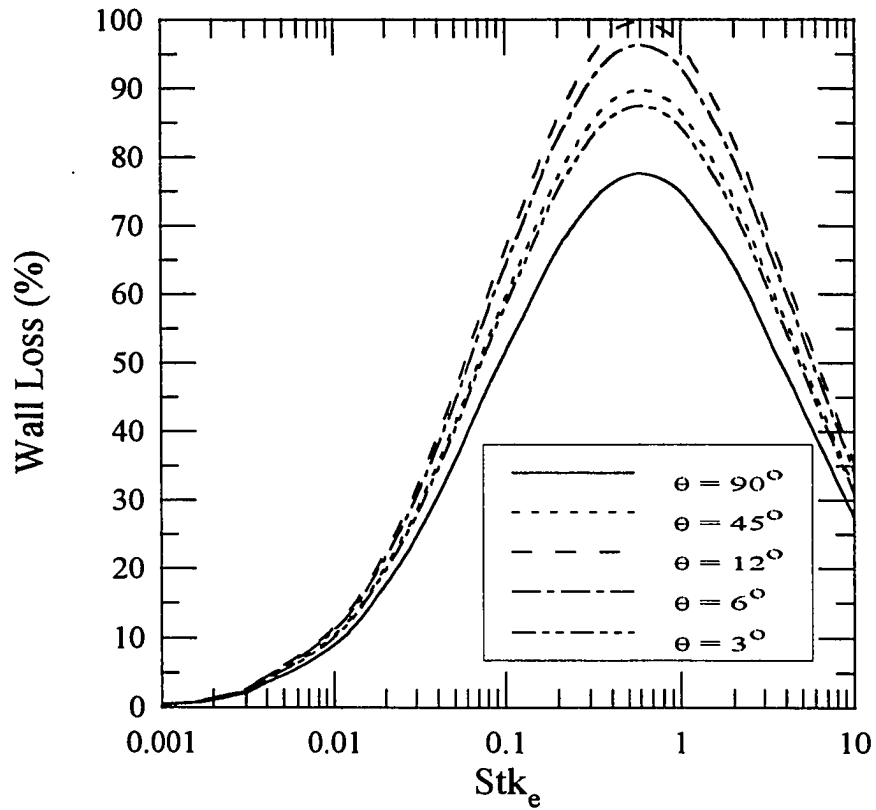


Figure 6.8. Wall loss for expansion fittings as predicted by Equation 6.2, $A_o/A_e = 16$.

expansion, a separation region is set up at a half-angle between 5° and 8° (Schlichting, 1979). Highest shear and turbulence production will take place at the boundary between the separation and the main flow. The separation region acts as a buffer region, keeping the particles away from the wall as they are pushed outward towards the wall by the shear layer. As the expansion angle decreases, the data of Chatuverdi (1963) shows that the separation regions gets narrower, thus lowering the shielding effect of the separation and causing more particles to strike the wall. However, as the angle becomes very small (less than $\sim 8^\circ$), the separation region disappears, the shear layer becomes weaker, and the radial component of velocity decreases as the angle continues to decrease. The weaker shear layer and lower radial velocity will cause less particles to strike the wall; hence, a decrease in aerosol losses as the expansion half-angle decreases below $\sim 8^\circ$.

Peak losses occur between values of Stk_e of 0.7 and 1.3, depending on the area ratio. The lower the area ratio, the higher the value of Stk_e at which peak losses will occur. For a given geometry, the particles are able to follow the flow stream lines when Stk_e is low; thus, the aerosol losses are low for small values of Stk_e . As Stk_e increases, the inertia of the particles increase. This increase in particle inertia will cause the particles to be less able to follow the flow streamlines and strike the wall; however, after Stk_e reaches a critical value (between 0.7 and 1.3 depending on the expansion half-angle), the inertia of the particles becomes large enough that the particles loose sensitivity to the disturbance caused by the expansion. The later effect will cause less particles to deposit as the Stokes number increases. Finally, as Stk_e becomes very large, the particles will be unaffected by the expansion and the effect of the expansion on particle deposition is greatly diminished.

CHAPTER VII

LARGE-DIAMETER TRANSPORT TUBES

The experimental results showing the non-dimensional deposition velocity as a function of the non-dimensional particle relaxation time are given in Figure 7.1. The error bars on the data points represent a 95% confidence interval about the mean of replicate tests at each set of experimental conditions. The uncertainties ranged from 3.2% to 182.0%. Details of the uncertainty calculation are presented in Appendix B. Data for the large-diameter transport tubes is included in tabular form in Appendix F. Because earlier studies have not included an uncertainty analysis, the geometric standard deviation, σ_g , will be used as a comparative measure with other studies. The geometric standard deviation of a set of v_+ values is defined by:

$$\ln v_{+,g} = \frac{1}{N} \sum_{i=1}^N \ln v_+ \quad (7.1)$$

where $v_{+,g}$ is the geometric mean and is defined as:

$$\ln^2 \sigma_g = \frac{1}{N-1} \sum_{i=1}^N (\ln v_+ - \ln v_{+,g})^2 \quad (7.2)$$

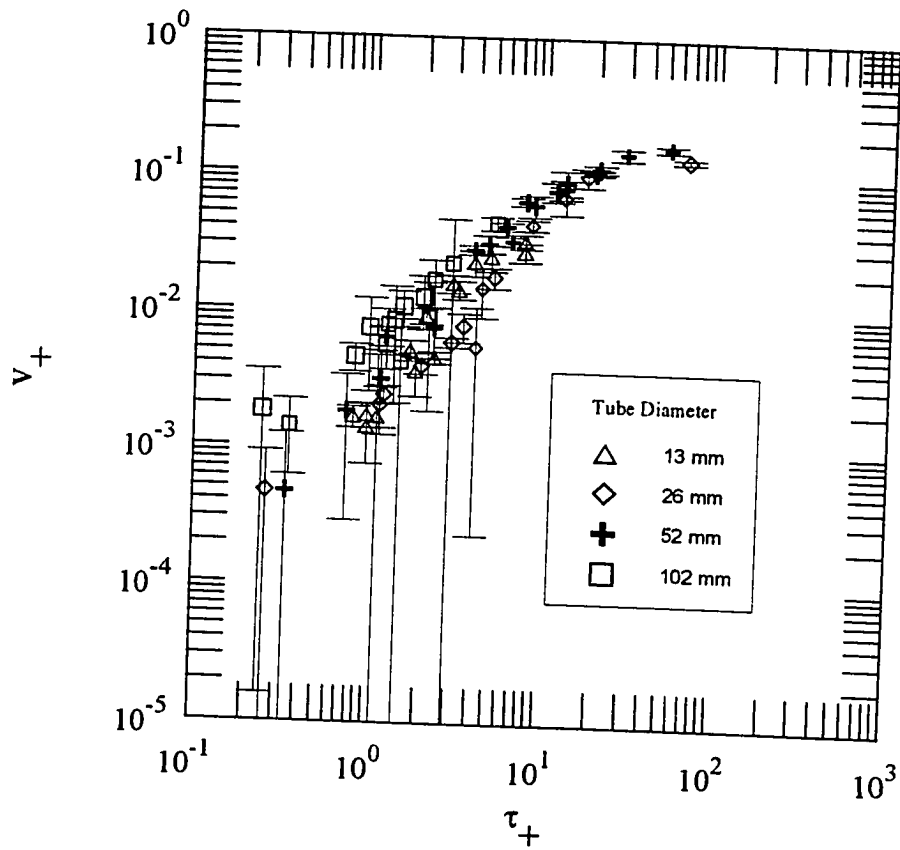


Figure 7.1. Non-dimensional deposition velocity as a function of non-dimensional particle relaxation time for various tube diameters.

The average of the geometric standard deviations for all test conditions is 1.13. In contrast, a plot by Onda (1977) of v_+ versus τ_+ for data that were available to him from the literature shows a geometric standard deviation of approximately 1.5 for τ_+ values that are on the order of 1 and a geometric standard deviation of approximately 2 for τ_+ values on the order of 0.1.

The non-dimensional deposition velocity, v_+ , was correlated with the flow Reynolds number, Re , and the dimensionless relaxation time, τ_+ , in the form of a sigmoid curve. Several sigmoid forms were tried, but the best correlation was obtained using the functional form:

$$v_+ = c_1 e^{-0.5 \left(\frac{Re - c_2}{c_3} \right)^2} + c_4 e^{-0.5 \left(\frac{\ln \tau_+ - \ln c_5}{c_6} \right)^2} \quad (7.3)$$

where the coefficients c_1 , c_2 , c_3 , c_4 , c_5 , and c_6 were fit by a least squares procedure. The resulting values of the coefficients are:

$$\begin{aligned} c_1 &= 2.26 \times 10^{-2} \\ c_2 &= 4.03 \times 10^4 \\ c_3 &= 1.533 \times 10^4 \\ c_4 &= 0.1394 \\ c_5 &= 49.0 \\ c_6 &= 1.136 \end{aligned}$$

The correlation coefficient, r^2 , of Equation 7.3 is 0.983.

Equation 7.3 essentially represents a surface in three dimensional space, and a plot of that surface is given in Figure 7.2. The surface covers the ranges of the independent variables of $0.1 \leq \tau_+ \leq 100$ and $2,500 \leq Re \leq 50,000$. In general terms, the correlation provides a better fit to the data than does a simple plot of v_+ versus τ_+ . As a comparison, if a sigmoid curve (of a different form than that used in Equation 7.3) were fit to the data of Figure 7.1, the correlation coefficient would be 0.968. Figure 7.3 is a plot of the non-dimensional deposition velocity as a function of the non-dimensional particle relaxation time for constant values of Reynolds number as predicted by Equation 7.3. It can be seen that v_+ increases with increasing Reynolds number for low τ_+ values. This is to be expected since turbulent diffusion increases with increasing Reynolds number. At higher Reynolds numbers, turbulent diffusion causes the particles to move towards the wall more readily and hence the higher deposition velocities. As τ_+ increases, the particles are less able react to the changes produced by the turbulent flow until finally, the deposition velocity becomes independent of the diffusion effects.

Given the dimensions of a vertical transport tube, the flow rate and aerodynamic particle size, Equations 2.2 and 7.3 can be used to calculate aerosol transmission through the tube. Plots of such calculations for the tubes used in the present experiments are shown in Figures 7.4-7.7 together with experimental data. Figure 7.4 shows the results for penetration of $10 \mu\text{m AD}$ aerosol particles through a 13 mm diameter by 2.7 m long tube; and, Figures 7.5 through 7.7 show results for the penetration of $20 \mu\text{m AD}$ aerosol particles through tubes that are 26 mm diameter by 2.7 m; 52 mm diameter by 2.7 m long by 102

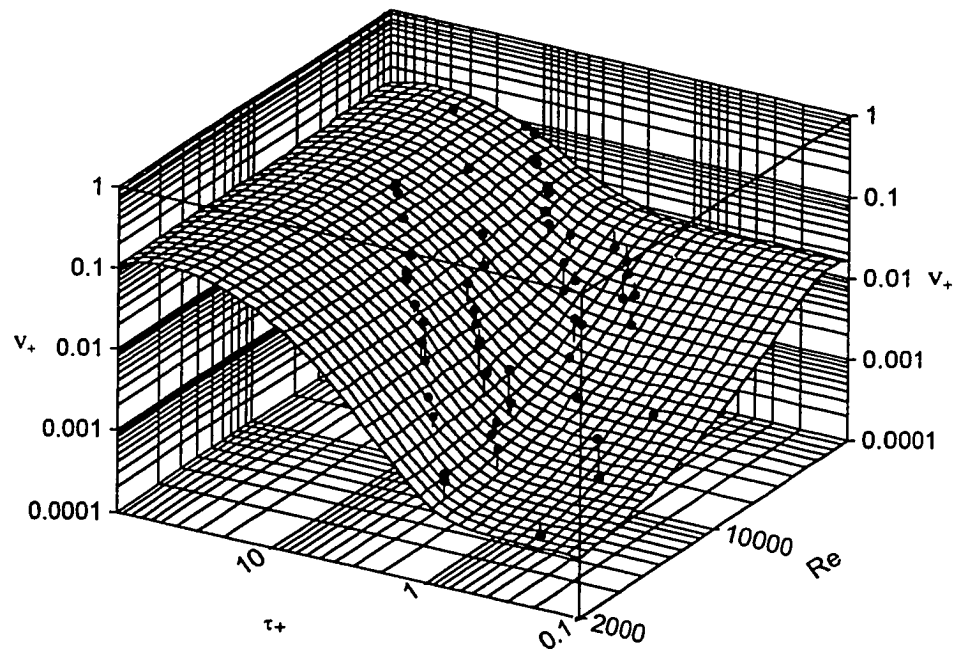


Figure 7.2. Correlation for large-diameter transport tubes.

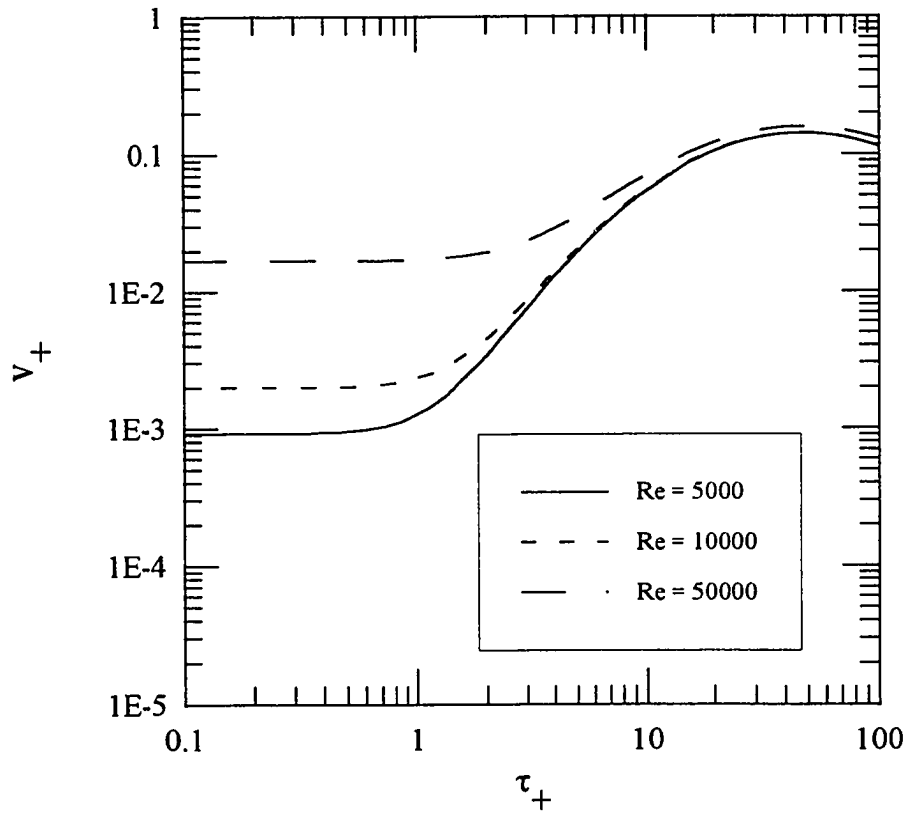


Figure 7.3. Non-dimensional deposition velocity as a function of non-dimensional particle relaxation time for constant Reynolds numbers.

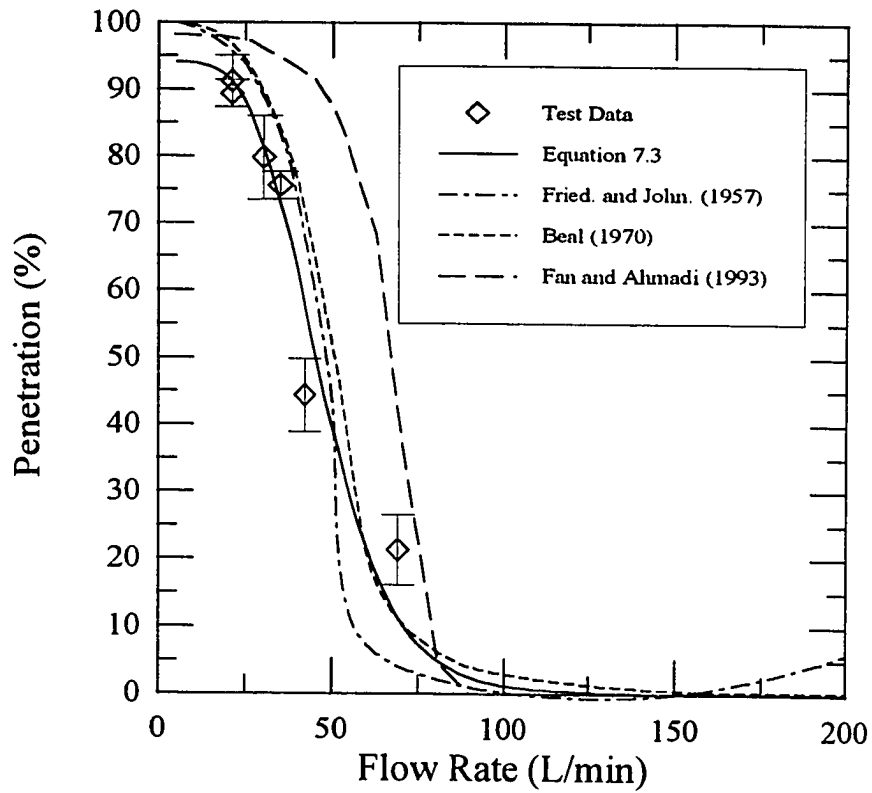


Figure 7.4. Penetration of 10 μm AD aerosol particles through a 13 mm diameter by 2.7 m long vertical tube.

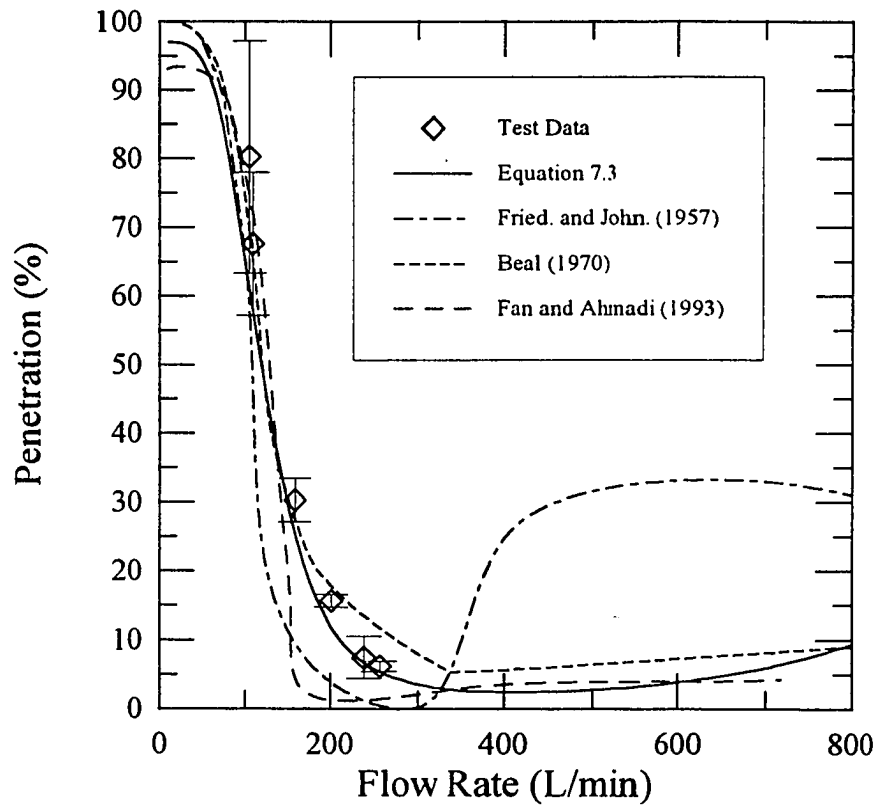


Figure 7.5. Penetration of 20 μm AD aerosol particles through a 26 mm diameter by 2.7 m long vertical tube.

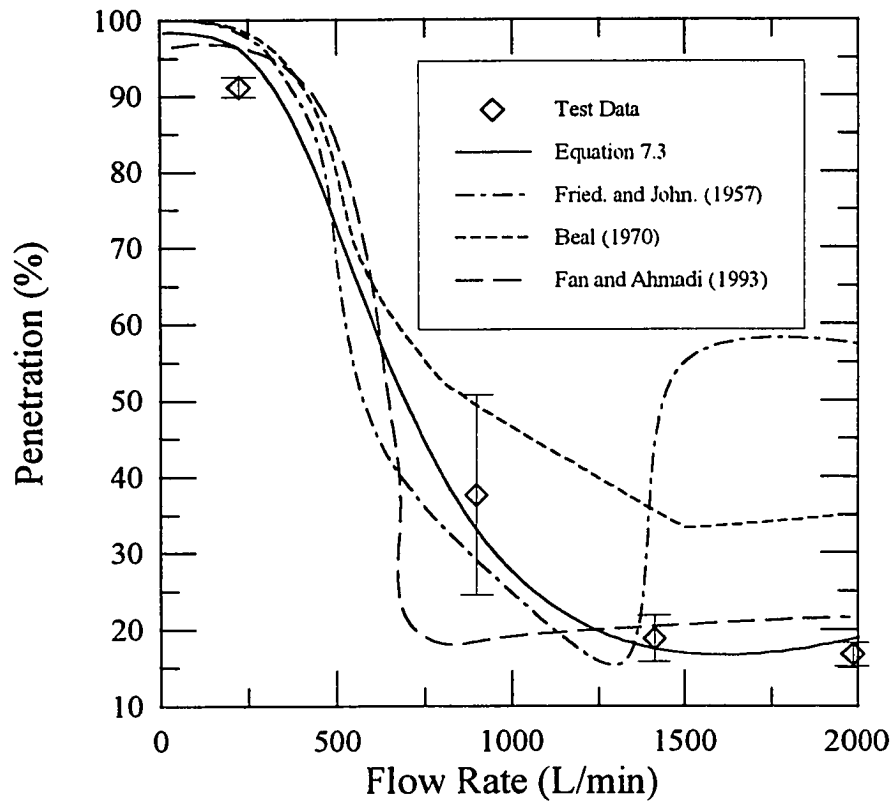


Figure 7.6. Penetration of 20 μm AD aerosol particles through a 52 mm diameter by 2.7 m long vertical tube.

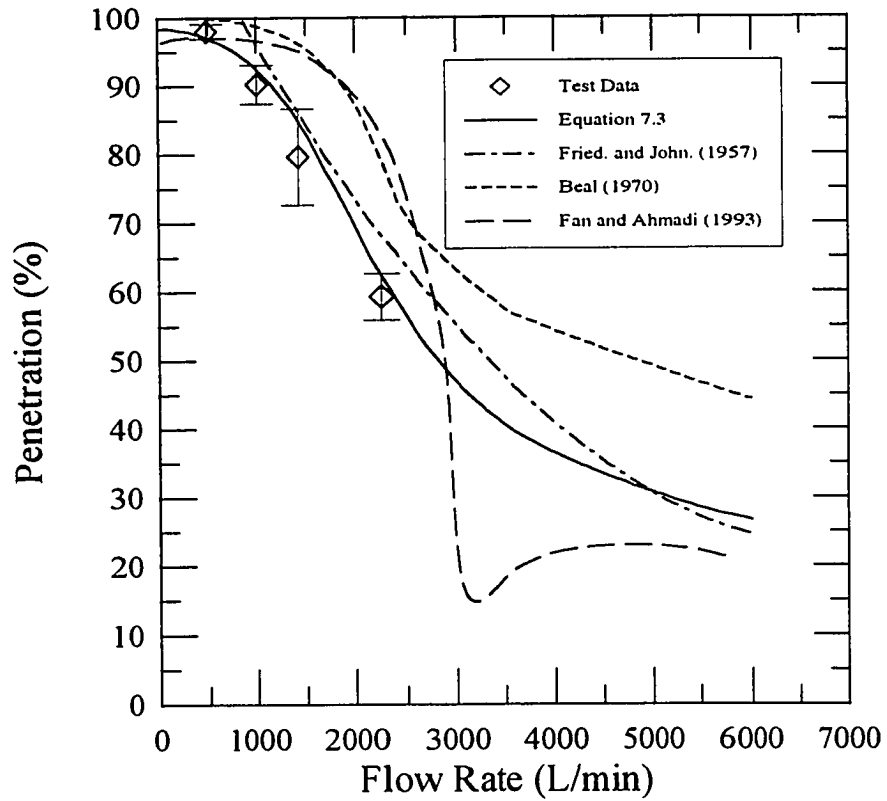


Figure 7.7. Penetration of 20 μm AD aerosol particles through a 102 mm diameter by 5.5 m long vertical tube.

mm diameter by 5.5 m long, respectively. The larger particle sizes and longer tube length were used in the experiments to increase deposition in the tube and, correspondingly improve experimental resolution in the larger tubes.

Although there have been many models proposed for turbulent deposition, three models have been chosen for comparison with the experimental data and correlation. Onda (1977) examined the models available at the time of his study and compared the predictions of those models with available experimental data. He concluded the model of Beal (1970) best fit the data. The Beal model is based on the free-flight stopping concept (Friedlander and Johnstone, 1957; Davies, 1966; Liu and Ilori, 1974; and, Papavergos and Hedley, 1984) and it gives results that are representative of that class of model. Beal's model and the model of Friedlander and Johnstone (1957) are compared to the test data in Figures 7.4-7.7. In the model of Friedlander and Johnstone (1957) the non-dimensional deposition velocity is calculated from the following equations:

$$v_* = \frac{\sqrt{\frac{f}{2}}}{\left[1 + \sqrt{\frac{f}{2} \left(\frac{1525}{S_*^2} - 50.6\right)}\right]} \quad \text{if } S_* < 5 \quad (7.4)$$

$$v_* = \frac{\sqrt{\frac{f}{2}}}{\left[1 + \sqrt{\frac{f}{2} \left\{5 \ln\left(\frac{5.04}{\frac{S_*}{5} - 0.959}\right) - 13.73\right\}}\right]} \quad \text{if } 5 \leq S_* \leq 30 \quad (7.5)$$

$$v_+ = \sqrt{\frac{f}{2}} \quad \text{if } S_+ > 30 \quad (7.6)$$

where: S_+ is the non-dimensional stopping distance and is given by :

$$S_+ = \frac{SV_+}{v} \quad (7.7)$$

and:

$$S = \frac{\rho_p D_p^2 U}{18\mu} + \frac{D_p}{2} \quad (7.8)$$

In Beal's model (1970), the non-dimensional deposition velocity is calculated from:

$$v_+ = \left(\frac{1}{Vs_+} + \frac{1}{K_+} \right) \quad (7.9)$$

where, Vs_+ is the dimensionless particle coasting velocity, and K_+ is the particle transport coefficient. The particle coasting velocity is given by:

$$Vs_+ = Vb_+ + \frac{v'_+(Dp_+/2) + v'_+(S_+)}{4} \quad (7.10)$$

Here: Vb_+ is the Brownian diffusion velocity given by:

$$Vb_+ = \left(\frac{3K_b T}{\pi D_p^2 \rho_p^3} \right)^{\frac{1}{2}} \frac{1}{V_+} \quad (7.11)$$

where K_b is the Boltzman's constant and T is the temperature of the fluid. The second term in Equation 7.8 is the arithmetic mean of the r. m. s. value of the radial component of the fluctuating gas velocity, v' , evaluated at a non-dimensional distance from the wall $y_+ = D_{p+}/2$ and at S_+ . The r. m. s. value of the radial component of fluctuating velocity is given by:

$$\begin{aligned} v'_{+}(y_+) &= 0.05 y_+ & (0 \leq y_+ \leq 10) \\ v'_{+}(y_+) &= 0.5 + 0.0125 (y_+ - 10) & (10 \leq y_+ \leq 30) \\ v'_{+}(y_+) &= 0.75 + 0.003 (y_+ - 30) & (y_+ \geq 30) \end{aligned} \quad (7.12)$$

The particle transport coefficient, K_+ , is calculated from:

$$\begin{aligned} \frac{1}{K_+} &= \frac{14.5}{3} Sc^{\frac{2}{3}} F(Sc, S_+) - \frac{14.5^2}{3R_+} Sc^{\frac{1}{3}} G(Sc, S_+) \\ &+ \left(5 + \frac{25}{R_+} \left\{ \frac{1}{Sc} - 0.959 \right\} \right) \ln \left(\frac{1+5.04 Sc}{1+0.04 Sc} \right) - \frac{125}{R_+} \\ &+ \frac{1 - 13.73 \sqrt{\frac{f}{2}}}{\sqrt{\frac{f}{2}}} \quad \text{if } 0 \leq S_+ \leq 5 \end{aligned} \quad (7.13)$$

$$\frac{1}{K_*} = \left(5 + \frac{25}{R_*} \left\{ \frac{1}{Sc} - 0.959 \right\} \right) \ln \left(\frac{1 + 5.04 Sc}{1 + Sc \left(\frac{S_*}{5} - 0.959 \right)} \right) \quad (7.14)$$

$$- \frac{25}{R_*} \left(6 - \frac{S_*}{5} \right) + \frac{1 - 13.73 \sqrt{\frac{f}{2}}}{\sqrt{\frac{f}{2}}} \quad \text{if } 5 \leq S_* \leq 30$$

$$\frac{1}{K_*} = \frac{1 - 13.73 \sqrt{\frac{f}{2}}}{\sqrt{\frac{f}{2}}} \quad \text{if } S_* \geq 30 \quad (7.15)$$

where:

$$F(Sc, S_*) = f(Sc, 5) - f(Sc, S_*) \quad (7.16)$$

$$G(Sc, S_*) = g(Sc, 5) - g(Sc, S_*) \quad (7.17)$$

and:

$$f(Sc, y_*) = \frac{1}{2} \ln \left(\frac{(1 + \gamma)^2}{1 - \gamma + \gamma^2} \right) + \sqrt{3} \tan^{-1} \left(\frac{2\gamma - 1}{\sqrt{3}} \right) \quad (7.18)$$

$$g(Sc, y_+) = \frac{1}{2} \ln \left(\frac{1 - \gamma + \gamma^2}{(1 + \gamma)^2} \right) + \sqrt{3} \tan^{-1} \left(\frac{2\gamma - 1}{\sqrt{3}} \right) \quad (7.19)$$

$$\gamma = \frac{y_+}{14.5} Sc^{\frac{1}{3}} \quad (7.20)$$

Here: Sc , is the Schmidt number and y_+ is the non-dimensional distance from the tube wall. Comparisons are also made in Figures 7.4-7.7 of the data and new model with the model of Fan and Ahmadi (1993). Their model was selected for comparison because it is representative of more recent models that are based on the particle trajectories in the turbulence coherent structures near the wall (Cleaver and Yates, 1975; Fichman et al., 1988). Fan and Ahmadi (1993) present the following equation for calculating the non-dimensional deposition velocity:

$$v_+ = 0.84 Sc^{-\frac{2}{3}} + \frac{1}{2} \left[\frac{\left(0.64 k_+ + \frac{Dp_+}{2} \right)^2 + \frac{\tau_+^2 g_+ L_+}{0.01085(1 + \tau_+^2 L_+)}}{3.42 + \frac{\tau_+^2 g_+ L_+}{0.01085(1 + \tau_+^2 L_+)}} \right] \quad (7.21a)$$

$$\times \frac{0.037 \left[1 + 8 e^{\left(\frac{-(\tau_+ - 10)^2}{32} \right)} \right]}{1 - \tau_+^2 L_+ \left(1 + \frac{g_+}{0.037} \right)} \quad \text{if } v_+ < 0.14$$

and:

$$v_* = 0.14 \quad \text{if } v_* \geq 0.14 \quad (7.21b)$$

Here: k_* is the non-dimensional surface roughness, D_{p*} is the non-dimensional particle diameter, g_* is the non-dimensional gravitational force, and L_* is the non-dimensional lift force.

For the 13 mm diameter tube; the new correlation, Beal's model, and Friedlander and Johnstone's model agree well with the experimental data. The model of Fan and Ahmadi overestimates penetration. For tube diameters larger than 26 mm, the deviations from the experimental data are significant for the Beal model, the Friedlander and Johnstone model, and the Fan and Ahmadi model. As an example, at a flow rate of 2,260 L/min in a 102 mm diameter tube, the measured penetration for 20 μm AD particles is $59.3 \pm 1.1\%$ and the penetration predicted by the present model is 62.5%. In contrast, the Beal model predicts a penetration of 80.2% and the Fan and Ahmadi model predicts a penetration of 82.2%. Very significant deviations are observed for the Friedlander and Johnstone model at higher flow rates. These differences are in the region for which the non-dimensional stopping distance is greater than 30, a region where Friedlander and Johnstone did not validate their model.

CHAPTER VIII

SUMMARY

If the performance of a transport system is to be accurately evaluated, the losses in each component of the transport system must be known. An empirical approach has been taken to model the aerosol deposition in contraction and expansion fittings. The correlation for the contraction fittings was based on 91 tests conducted for two area ratios with a range of particle diameters and contraction half-angles. The correlation was fitted to the data over the range of $0.001 \leq Stk_c (1 - A_o/A_c) \leq 100$ and $12^\circ \leq \theta \leq 90^\circ$ and has a correlation coefficient of 0.987. The correlation for the expansion fittings was based on 128 tests conducted for a range of expansion angles, area ratios, particle diameters, and flow rates. The correlation fits the data with a correlation coefficient, r^2 , of 0.960 and covers the range of independent parameters of $0.001 \leq Stk_c \leq 10$, $1.7 \leq A_o/A_c \leq 16$, and $3^\circ \leq \theta \leq 90^\circ$.

If continuous monitoring is performed on a stack or duct, the losses of aerosol in the transport line should be small. For vertical sections of tubing, there can be considerable benefit in using large transport lines to improve aerosol penetration; however, it should be noted that for horizontal tubes, the use of larger sized tubes may cause increased sedimentation losses and an overall decrease in penetration (Anand et al., 1989). Ström (1989) has utilized the large-tube principal for continuous monitoring from nuclear stacks, where there can be long vertical runs.

To effectively model the penetration of aerosols through a large tube, the deposition velocity must be known. A correlation for predicting the non-dimensional deposition

velocity has been developed based on the results of 56 tests conducted with a range of tube sizes and particle diameters. The correlation includes the Reynolds number to account for turbulent diffusion effects not reflected by the non-dimensional particle relaxation time. The correlation fits the data over the range of $0.1 \leq \tau_p \leq 100$ and $2500 \leq Re \leq 50,000$ with a correlation coefficient of 0.983. Use of the present model shows better agreement with experimental data than do predictions from use of previous models. This is particularly noticeable for the largest tube size tested (high Reynolds numbers), where the previous models overestimate penetration. This is also the region where turbulent diffusion effects would be of consequence.

The correlations for contraction fittings, expansion fittings, and large-diameter transport tubes presented in this study should be useful engineering tools for predicting the aerosol losses in sampling systems that make use of such components. These sub-models should be incorporated into the DEPOSITION code to enhance its prediction capabilities.

REFERENCES

- American National Standards Institute (1969). *Guide to Sampling Airborne Radioactive Materials in Nuclear Facilities*. ANSI Standard N13.1-1969. New York: American National Standards Institute.
- American Society of Mechanical Engineers (1985). *Measurement Uncertainty, Instruments And Apparatus. Part 1* (ANSI/ASME PTC 19.1-1985). New York: The American Society of Mechanical Engineers.
- Anand, N.K. and McFarland, A.R. (1989). *Am. Ind. Hyg. Assoc. J.* 50:307-312.
- Anand, N. K.; McFarland, A. R. and Kocmoud, C. J. (1993). *DEPOSITION: Software to Calculate Particle Penetration Through Aerosol Transport Systems*. U.S. Nuclear Regulatory Commission Report NUREG/GR-006. US Government Printing Office, Washington, DC.
- Beal, S. K. (1970). *Nuclear Sci. and Eng.* 40:1-11.
- Berglund, R.N. and Liu, B.Y.H. (1973). *Environ. Sci. Technol.* 7:147-153.
- Chatuverdi, M. C. (1963). *J. of Hydraulics Division* 89:61-92.
- Chen, D. and Pui, D. Y. H. (1995). *J. Aerosol Sci.* 26:563-574
- Cleaver, J. W. and Yates, B. (1975). *Chem. Eng. Sci.* 30:983-992.
- Davies, C. N. (1966). Deposition from Moving Aerosols. In: *Aerosol Science*, C.N. Davies, ed. New York: Academic Press.
- Fan, F. and Ahmadi, G. (1993). *J. Aerosol Sci.* 24: 45-64.
- Farmer, R.; P. Griffith, and Rohsenow, W. M. (1970). *J. Heat Trans.* 92:587-601.
- Fichman, M.; Gutfinger, C. and Pnueli, D. (1988). *J. Aerosol Sci.* 19: 123-136.

- Fluid Dynamics International, Inc.(1993). *FIDAP User's Manual, Revision 7.0*. Evanston, IL.
- Forney, L.J. and Spielman, L.A. (1974). *Aerosol Sci.* 5:257-271.
- Friedlander, S. K. and Johnstone, H. T. (1957). *Ind. Eng. Chem.* 49: 1151-1156.
- Fuchs, N. A. (1964). *Mechanics of Aerosols*. New York: Pergamon Press.
- Gong, H.; Anand, N. K. and McFarland, A. R. (1993). *Aerosol Sci. and Technol.* 19:294-304.
- Hardalupas, Y.; Taylor, A. M. K. P.; and Whitelaw, J. H. (1992). *Phil. Trans. R. Soc. Lond. A.* 341:411-442.
- Ilori, T. A. (1971). Turbulent Deposition of Particles Inside Pipes. Ph.D. Dissertation, University of Minnesota, Minneapolis, MN.
- Itoh, H.; Smaldone, G. C.; Swift, D. L. and Wagner, H. N. (1985). *J. Aerosol Sci.* 16:167-174.
- Kanaoka, C.; Emi, H. and Aikura, T. (1979). *J. Aerosol Sci.* 10:29-41.
- Kim, C. S.; Lewars, G. G.; Eldrige, M. A. and Sacker, M. A. (1984). *J. Aerosol Sci.* 15:167-176
- Kindler, P.;Elliot, M. A.; Stephenson, B. K. and Matteson, M. J. (1991). *J. Aerosol Sci.* 22: 259-266.
- Laufer, J. (1953). *The Structure of Turbulence in Fully Developed Pipe Flow*. NACA Report 2954. National Bureau of Standards, Washington, DC.
- Liu, B. Y. H. and Agarwal, J. K. (1974). *Aerosol Sci.* 5:145-166.
- Liu, B. Y. H. and Ilori, T. A. (1974). *Environ. Sci. & Technol.* 8:351-356.

- Olan-Figueroa, E., A. R. McFarland, and C. A. Ortiz (1982). *Am. Ind. Hyg. Assoc.* 43:395-399.
- Onda, K. (1977). *A Review of Theoretical and Experimental Studies of Particle Deposition in Turbulent*. High Temperature Gas Dynamics Laboratory, Flow Memorandum Report No. 7, Mechanical Engineering Department, Stanford University, Palo Alto, CA.
- Papavergos, P. G. and Hedley, A. B. (1984). *Chem. Eng. Res. Dds.* 62: 275-295.
- Pich, J. (1964). *Coll. Czech. Chem. Commun.* 29:2223-2227
- Postma, A. K. and Schwendiman, L. C. (1960). *Studies in Micrometrics: Particle Deposition in Conduits as a Source of Error in Aerosol Sampling*. Hanford Lab Report HW 65308. Richland, WA.
- Schlichting, H. (1979). *Boundary Layer Theory*. New York: McGraw-Hill Book Co.
- Sehmel, G. A (1970). *J. Geophys. Res.* 75:1766-1781.
- Smith, T. N. and Phillips, C. R. (1975). *Environ. Sci. Technol.* 9:564-568.
- Smutek, M. and Pich, J. (1974). *Aerosol Sci.* 5:17-24.
- Sommerfeld, M.; Ando, A. and Wenneberg, D. (1992). *J. of Fluids Eng.* 114:648-656.
- Ström, L. (1989). *The Measurement of Power Reactor Stack Releases Under Accident Conditions*. Report Studsvik/NS-89/18. Studsvik Nuclear, Studsvik AB, Sweden.
- Tennekes, H. and Lumley, J. L. (1992). *A First Course in Turbulence*. Cambridge, MA: The MIT Press.
- U.S. Environmental Protection Agency (1994a). National Emissions Standards for Emissions of Radionuclides other than Radon from Department of Energy Facilities.

40 CFR 61 Sub-Part H. *Code of Federal Regulations*. US Government Printing Office, Washington, DC 20402.

U.S. Environmental Protection Agency (1994b). National Emissions Standards for Emissions of Radionuclides from Facilities Licensed by the Nuclear Regulatory Commission and Federal Facilities not Covered by Sub-Part H. 40 CFR 61 Sub-Part I. *Code of Federal Regulations*. US Government Printing Office, Washington, DC.

U.S. Environmental Protection Agency. (1994c) Letter from Ms. Mary D. Nichols, Assistant Administrator for Air and Radiation, U.S. EPA to Mr. Raymond F. Pelletier, Director, Office of Environmental Guidance, U.S. DOE; dated November 21, 1994. (Personal collection, A. Muyschondt)

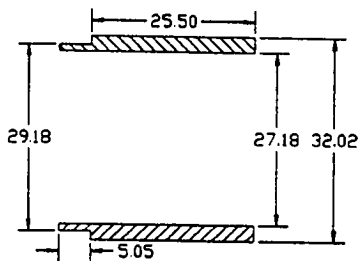
U.S. Nuclear Regulatory Commission (1992). Air Sampling in the Workplace. *Nuclear Regulatory Guide 8.25*. US Government Printing Office, Washington, DC 20402.

U.S. Statutes at Large (1990). Clean Air Act Amendment Act of 1990. Public Law 101-549. 104:Part 4. US Government Printing Office, Washington, DC.

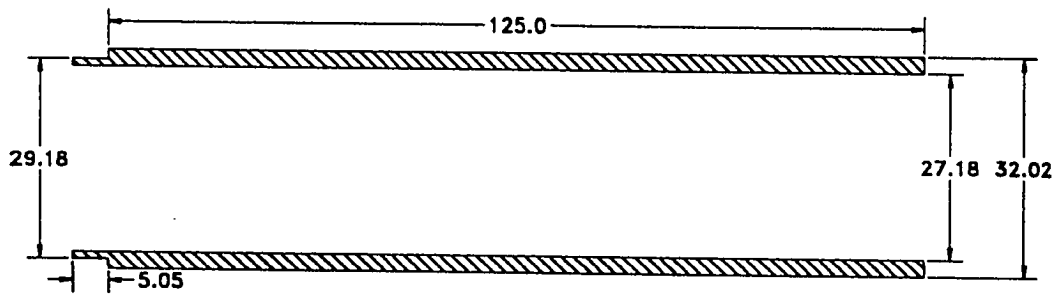
Wells, A. C. and Chamberlain, A. C. (1967). *Brit. J. App. Phys.* 18:1793.

Ye , Y. and Pui, D. Y. H. (1990). *J. Aerosol Sci.* 21:29-40.

APPENDIX A
DETAILED DRAWINGS FOR CONTRACTION AND EXPANSION FITTINGS



a) Extension for contraction fittings.



b) Extension for expansion fittings.

Figure A.1. Extension pieces used for testing expansion and contraction fittings.

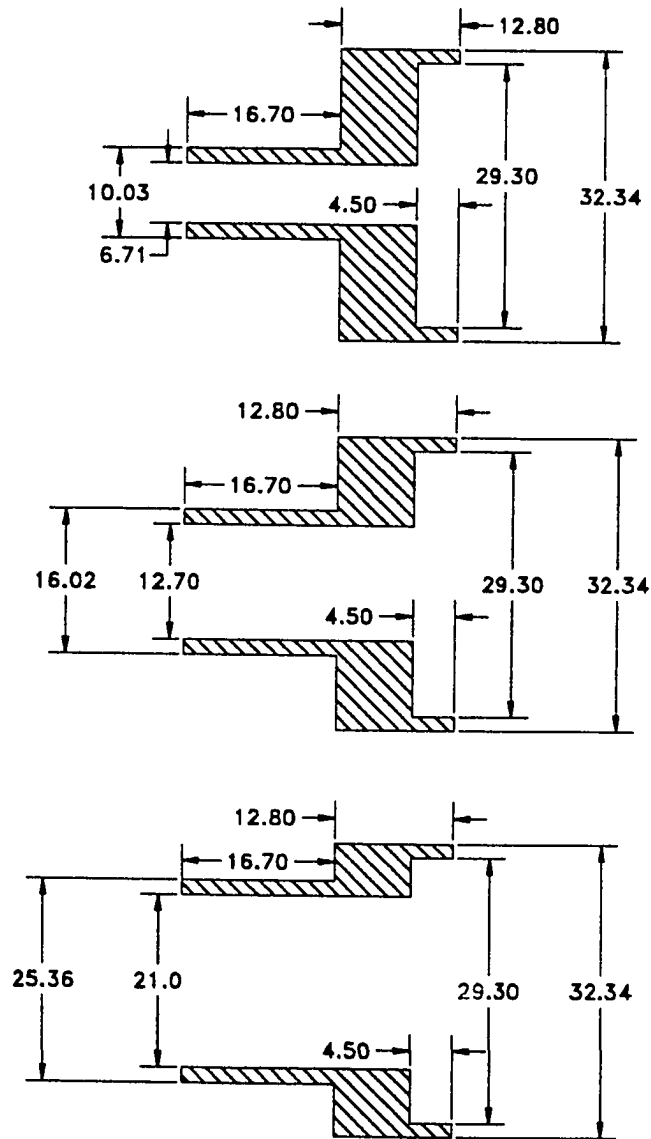


Figure A.2. Detailed drawings for the 90° fittings.

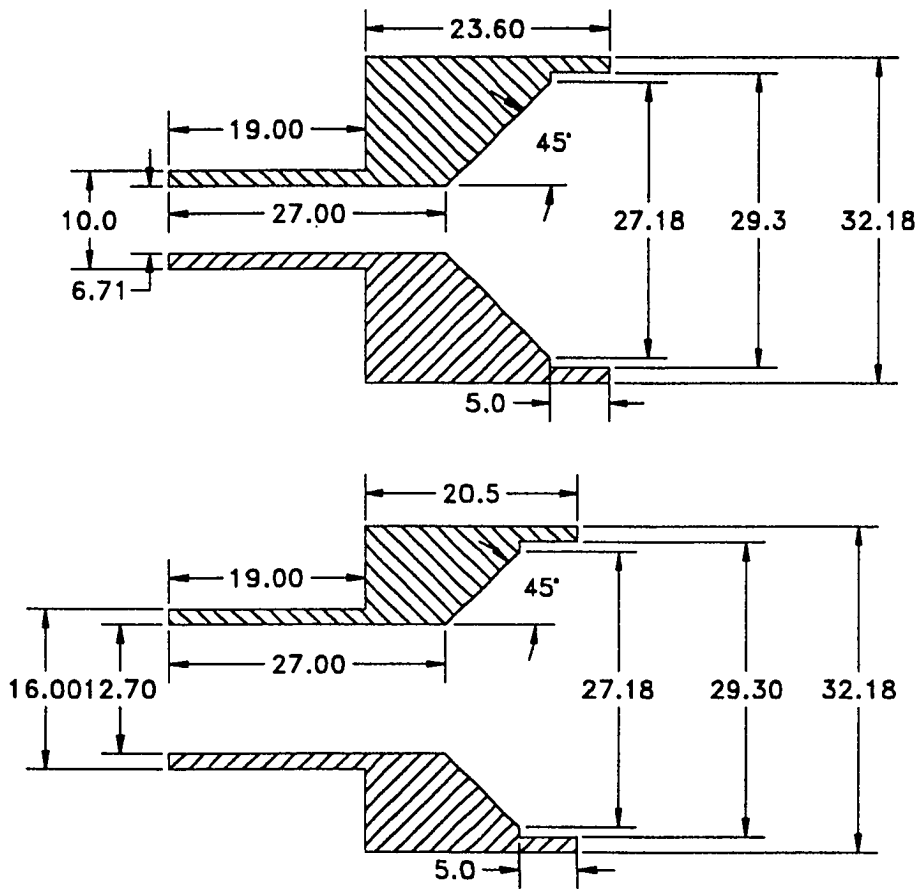


Figure A.3. Detailed drawings for the 45° fittings.

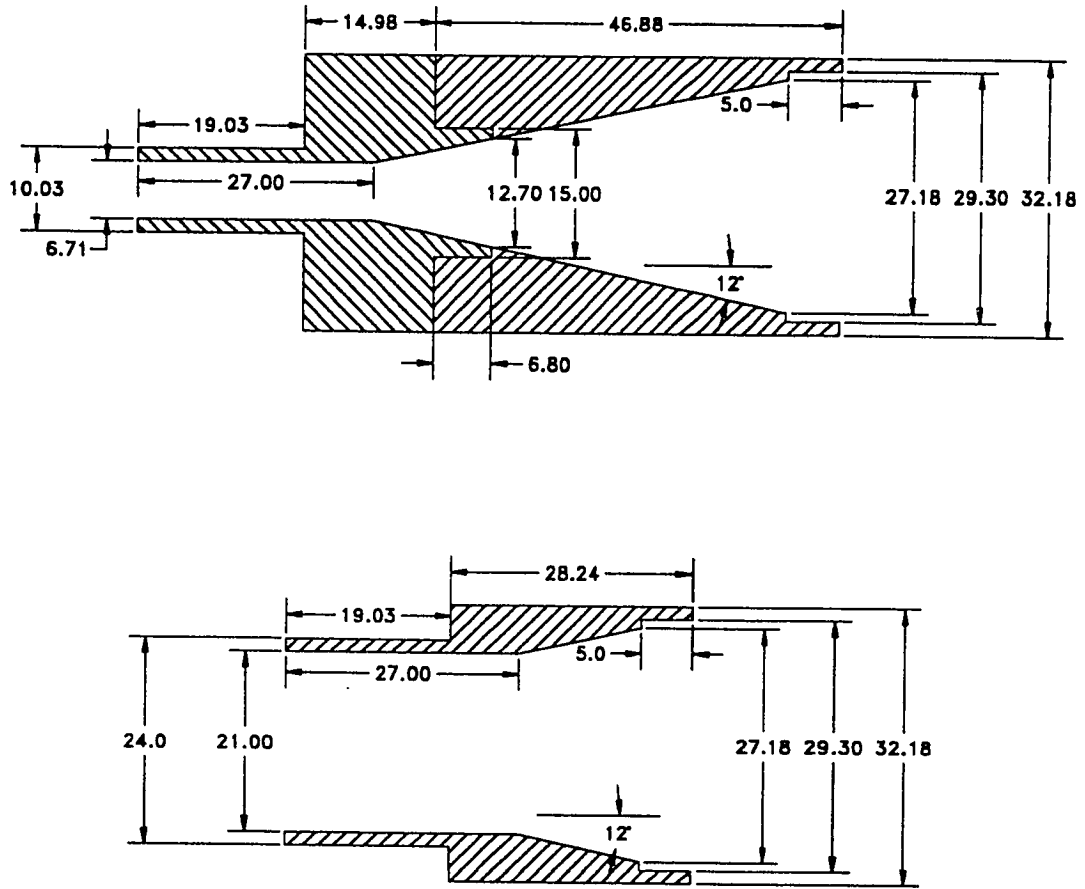


Figure A.4. Detailed drawings for the 12° fittings.

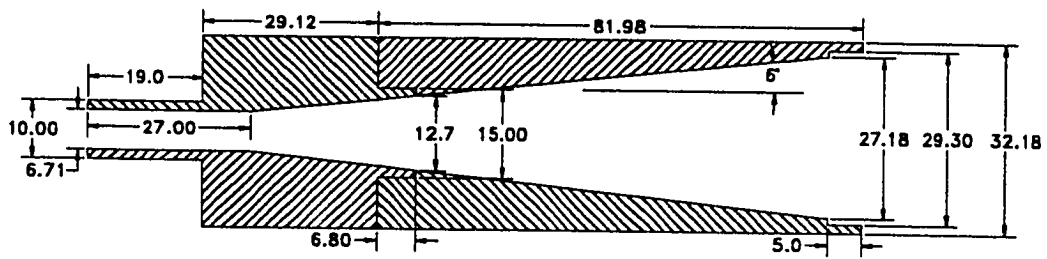


Figure A.5. Detailed drawings for the 6° fittings.

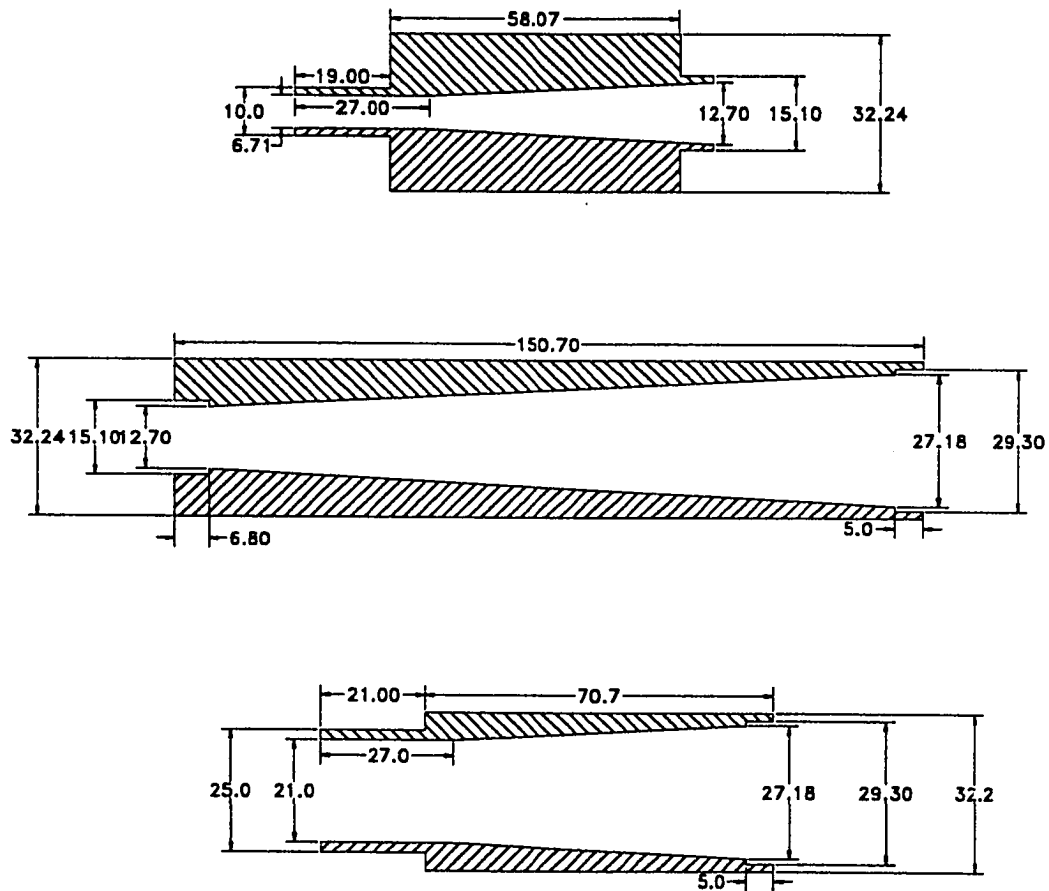


Figure A.6. Detailed drawings for the 3rd fittings.

APPENDIX B
UNCERTAINTY ANALYSIS

Uncertainty analysis is a very important part of any experimental study because it gives a measure of confidence for the results. The experimental uncertainty for this study will be performed following the ANSI/ASME PTC 19.1-1985 (1985) standard. According to the standard, the uncertainty, U_n , for 95% coverage of a result, R , that is expressed in terms of the average values G_i of the independent parameters is given by:

$$\frac{U_n}{R} = [B_r^2 + (tS_r)^2]^{\frac{1}{2}} \quad (\text{B.1})$$

where t is the two tailed student t -value and the other parameters are defined as follows:

$$B_r = \left[\sum_{i=1}^n \left(\frac{\delta_i B_i}{G_i} \right)^2 \right]^{\frac{1}{2}} \quad (\text{B.2})$$

and

$$S_r = \left[\sum_{i=1}^n \left(\frac{\delta_i S_i}{G_i} \right)^2 \right]^{\frac{1}{2}} \quad (\text{B.3})$$

where B_i is the bias limit of the result, S_i is the standard deviation of the result, n is the number of observations in the data set, and δ_i is the sensitivity parameter given by:

$$\delta_i = \frac{\partial R}{\partial G_i} \frac{G_i}{R} \quad (\text{B.4})$$

The bias limit is an estimate of the maximum probable value of its fixed error. The degrees of freedom for the student t -value distribution are $n-1$.

The standard deviation is calculated by:

$$S_i = \left(\frac{1}{n-1} \sum_{i=1}^n (X_i - G_i)^2 \right)^{\frac{1}{2}} \quad (\text{B.5})$$

where X_i is the individual measurement.

For the contraction fittings and the expansion fittings, the uncertainty for the wall loss is calculated as follows:

The wall loss is given by Equation 4.3 as:

$$WL = 1 - P \quad (\text{B.6})$$

The sensitivity parameter as given by Equation B.5 is determined to be:

$$\delta_P = -1 \frac{P}{WL} \quad (\text{B.7})$$

The bias limit of the penetration is 1% based on the linearity of the fluorometer, thus establishing the value for B_p . Four values for penetration were measure, this gives 3 degrees of freedom for determining the student *t-value*. For a 95% confidence interval and 3 degrees of freedom, the value for the student *t-value* is 3.182. For a penetration value of 85% with a standard deviation of 2, the uncertainty is then calculated by Equations B.1-B.4:

$$\frac{U_n}{WL} = \left[(-1 \times 0.01)^2 + \left(3.182 \times -1 \times \frac{1.9}{90.4} \right)^2 \right]^{0.5} = 0.0676 \text{ or } 6.76\%$$

In order to carry out the uncertainty analysis for the non-dimensional deposition velocity, it is more convenient to express it in terms of constants and directly measured parameters so that:

$$v_* = 1.296442 \frac{d_t^{7/8} \rho^{1/8} Q^{1/8} \ln\left(\frac{1}{P}\right)}{L \mu^{1/8}} \quad (\text{B.8})$$

The non-dimensional sensitivity parameters for the non-dimensional deposition velocity can then be determined by differentiating equation B.8:

$$\begin{aligned} \delta_\rho &= \frac{1}{8} \frac{\rho}{v_*}, \quad \delta_P = \frac{1}{\ln(P)} \frac{P}{v_*}, \quad \delta_{d_t} = \frac{7}{8} \frac{d_t}{v_*}, \\ \delta_Q &= \frac{1}{8} \frac{Q}{v_*}, \quad \delta_\mu = -\frac{1}{8} \frac{\mu}{v_*}, \quad \delta_L = -1 \frac{L}{v_*}. \end{aligned} \quad (\text{B.9})$$

Based on the accuracy to which the instrumentation can be read, the bias limits for the d_t and L were taken as 0.25%; for ρ and μ , 0.5%; 2% for Q , and 1% for P based on the linearity of the fluorometer. Four measurements were taken for each data point, giving 3 degrees of freedom for the student *t-value*. For a 95% confidence interval and 3 degrees of freedom, the student *t-value* is 3.182. For example, for a 13 mm ID and 2.7 m long tube with a penetration of 21% and standard deviation of 1.6, the uncertainty for the non-dimensional deposition velocity would be:

$$\begin{aligned}
\frac{U_n}{v_*} &= \left[\left(\frac{1}{8} \times 0.005 \right)^2 + \left(\frac{1}{8} \times 0.005 \right)^2 + \left(\frac{1}{8} \times 0.02 \right)^2 + \left(\frac{7}{8} \times 0.0025 \right)^2 \right. \\
&\quad \left. + (-1 \times 0.0025)^2 + \left(\frac{1}{\ln(0.21)} \times 0.01 \right)^2 + \left(3.182 \times \frac{1}{\ln(0.21)} \times \frac{2}{21} \right)^2 \right]^{0.5} \\
&= 0.194 \text{ or } 19.4\%
\end{aligned}$$

It should be noted that as the penetration approaches unity, the associated uncertainties will be dominated by the δ_p term and will be very large. This is due to the fact that as the penetration approaches unity, $1/\ln(P)$ approaches infinity.

APPENDIX C
EXPERIMENTAL DATA FOR CONTRACTION FITTINGS

TABLE C.1. Experimental Data for 90° Contraction Fittings.

Stk _c	Outlet I.D. (mm)	Entrance I. D. (mm)	D _p (μm)	Half- Angle (deg.)	P (%)	Uncert. (%)
0.009	6.2	27.2	5.9	90.0	97.0	3.9
0.043	6.2	27.2	5.9	90.0	98.7	3.3
0.082	6.2	27.2	5.9	90.0	95.5	1.4
0.160	6.2	27.2	5.9	90.0	84.4	6.9
0.029	6.2	27.2	10.6	90.0	98.5	9.1
0.138	6.2	27.2	10.6	90.0	92.0	11.0
0.262	6.2	27.2	10.6	90.0	74.7	7.7
0.511	6.2	27.2	10.6	90.0	57.2	14.2
0.054	6.2	27.2	14.6	90.0	96.2	5.2
0.261	6.2	27.2	14.6	90.0	78.1	10.5
0.495	6.2	27.2	14.6	90.0	57.9	2.5
0.977	6.2	27.2	14.6	90.0	38.0	8.9
2.500	6.2	27.2	19.7	90.0	19.2	12.0
1.797	6.2	27.2	19.7	90.0	22.6	6.5
0.488	6.2	27.2	19.7	90.0	58.3	5.6
0.004	12.7	27.2	5.9	90.0	98.3	4.3
0.021	12.7	27.2	5.9	90.0	97.7	2.0
0.040	12.7	27.2	5.9	90.0	95.9	3.5
0.083	12.7	27.2	5.9	90.0	90.8	7.4
0.014	12.7	27.2	10.6	90.0	99.0	1.7
0.067	12.7	27.2	10.6	90.0	96.1	7.2
0.128	12.7	27.2	10.6	90.0	90.2	2.1
0.263	12.7	27.2	10.6	90.0	76.4	4.0
0.026	12.7	27.2	14.6	90.0	95.8	9.2
0.127	12.7	27.2	14.6	90.0	88.3	2.0
0.241	12.7	27.2	14.6	90.0	77.5	2.1
0.493	12.7	27.2	14.6	90.0	61.2	5.8
0.047	12.7	50.8	16.4	90.0	100.0	1.1
0.139	12.7	50.8	16.4	90.0	90.0	2.2
0.286	12.7	50.8	16.4	90.0	74.2	3.3
0.116	12.7	50.8	21	90.0	92.0	5.3
0.228	12.7	50.8	21	90.0	78.3	2.8
0.467	12.7	50.8	21	90.0	60.3	5.3

TABLE C.2. Experimental Data for 45° Contraction Fittings.

Stk _c	Outlet I.D. (mm)	Entrance I. D. (mm)	D _p (μm)	Half- Angle (deg.)	P (%)	Uncert. (%)
0.673	6.7	27.2	9.8	45.0	70.9	15.0
0.334	6.7	27.2	9.8	45.0	90.6	4.5
0.225	6.7	27.2	9.8	45.0	95.4	1.9
0.521	6.7	27.2	10.2	45.0	75.9	4.1
0.649	6.7	27.2	10.2	45.0	70.3	7.8
0.556	6.7	27.2	10.2	45.0	73.8	5.8
0.412	6.7	27.2	10.2	45.0	81.8	11.0
0.105	6.7	27.2	10.2	45.0	99.4	2.1
1.214	6.7	27.2	16.4	45.0	53.3	2.2
0.676	6.7	27.2	16.4	45.0	72.7	13.8
0.173	6.7	27.2	16.4	45.0	97.7	3.8
1.954	6.7	27.2	16.7	45.0	42.4	10.8
1.547	6.7	27.2	16.7	45.0	47.0	10.0
1.264	6.7	27.2	16.7	45.0	49.9	3.6
0.963	6.7	27.2	16.7	45.0	57.2	2.5
0.651	6.7	27.2	16.7	45.0	70.0	6.4
0.326	6.7	27.2	16.7	45.0	91.2	1.9
3.337	6.7	27.2	23.1	45.0	31.4	14.3
1.258	6.7	27.2	23.1	45.0	53.7	5.8
0.620	6.7	27.2	23.1	45.0	77.8	2.7
0.925	6.7	27.2	23.1	45.0	62.8	4.0
2.143	12.7	27.2	24.6	45.0	40.0	4.4
1.093	12.7	27.2	24.6	45.0	59.4	3.4
0.736	12.7	27.2	24.6	45.0	70.6	1.4
0.186	12.7	27.2	24.6	45.0	96.7	3.4
0.116	12.7	50.8	20.8	45.0	98.7	1.3
0.228	12.7	50.8	20.8	45.0	94.6	3.5
0.467	12.7	50.8	20.8	45.0	82.7	1.9

TABLE C.3. Experimental Data for 12" Contraction Fittings.

Stk _c	Outlet I.D. (mm)	Entrance I. D. (mm)	D _p (μm)	Half- Angle (deg.)	P (%)	Uncert. (%)
2.535	6.2	27.2	19.7	12.0	62.2	2.9
1.797	6.2	27.2	19.7	12.0	67.7	6.4
0.488	6.2	27.2	19.7	12.0	89.7	2.5
0.495	6.2	27.2	14.6	12.0	89.5	2.8
0.976	6.2	27.2	14.6	12.0	78.6	11.1
0.029	6.2	27.2	10.6	12.0	99.5	1.7
0.138	6.2	27.2	10.6	12.0	98.2	3.9
0.262	6.2	27.2	10.6	12.0	96.2	2.6
0.512	6.2	27.2	10.6	12.0	86.6	2.0
0.755	6.2	27.2	10.6	12.0	81.4	8.6
0.701	6.2	27.2	10.6	12.0	82.9	4.3
0.640	6.2	27.2	10.6	12.0	84.8	3.8
0.599	6.2	27.2	10.6	12.0	85.2	4.8
0.532	6.2	27.2	10.6	12.0	87.4	3.0
0.485	6.2	27.2	10.6	12.0	88.9	15.9
0.411	6.2	27.2	10.6	12.0	89.6	1.9
0.360	6.2	27.2	10.6	12.0	93.0	4.7
0.477	6.2	27.2	10.6	12.0	90.1	8.4
0.241	6.2	27.2	10.6	12.0	96.5	2.0
0.124	6.2	27.2	10.6	12.0	99.2	2.0
0.517	6.2	27.2	10.6	12.0	87.3	4.1
0.262	6.2	27.2	10.6	12.0	95.3	2.4
0.162	6.2	27.2	5.9	12.0	98.5	1.8
0.086	12.7	27.2	5.9	12.0	99.9	1.5
0.008	12.7	27.2	10.3	12.0	99.2	2.0
0.064	12.7	27.2	10.3	12.0	99.6	5.5
0.121	12.7	27.2	10.3	12.0	98.6	2.7
0.250	12.7	27.2	10.3	12.0	96.8	5.8
0.241	12.7	27.2	14.6	12.0	96.0	4.7
0.491	12.7	27.2	14.6	12.0	90.5	3.1

APPENDIX D
NUMERICAL DATA FOR CONTRACTION FITTINGS

TABLE D.1. Numerical Data for 90° Contraction Fittings.

Stk _c	Outlet I.D. (mm)	Entrance I. D. (mm)	D _p (μm)	Half- Angle (deg.)	P (%)
0.104	6.4	25.4	5.0	90.0	83.6
0.408	6.4	25.4	10.0	90.0	63.3
1.621	6.4	25.4	20.0	90.0	18.1
0.195	6.4	25.4	5.0	90.0	70.5
0.769	6.4	25.4	10.0	90.0	41.8
3.051	6.4	25.4	20.0	90.0	15.1
0.052	12.7	25.4	5.0	90.0	90.5
0.204	12.7	25.4	10.0	90.0	84.1
0.810	12.7	25.4	20.0	90.0	53.2
0.098	12.7	25.4	5.0	90.0	91.4
0.384	12.7	25.4	10.0	90.0	71.1
1.525	12.7	25.4	20.0	90.0	40.5
0.065	19.1	25.4	5.0	90.0	91.3
0.256	19.1	25.4	10.0	90.0	85.4
1.017	19.1	25.4	20.0	90.0	69.5
1.525	12.7	50.8	20.0	90.0	34.4
0.384	12.7	50.8	10.0	90.0	76.7
0.098	12.7	50.8	5.0	90.0	85.0

TABLE D.2. Numerical Data for 45° Contraction Fittings.

Stk _c	Outlet I.D. (mm)	Entrance I. D. (mm)	D _p (μm)	Half- Angle (deg.)	P (%)
0.104	6.4	25.4	5.0	45.0	92.0
0.408	6.4	25.4	10.0	45.0	82.9
1.621	6.4	25.4	20.0	45.0	52.1
3.636	6.4	25.4	30.0	45.0	30.6
0.195	6.4	25.4	5.0	45.0	92.9
0.769	6.4	25.4	10.0	45.0	72.2
3.051	6.4	25.4	20.0	45.0	30.9
6.845	6.4	25.4	30.0	45.0	22.9
0.102	19.1	25.4	5.0	45.0	95.6
0.400	19.1	25.4	10.0	45.0	90.8
1.585	19.1	25.4	20.0	45.0	62.2
0.384	12.7	25.4	10.0	45.0	93.6
1.525	12.7	25.4	20.0	45.0	49.7
3.423	12.7	25.4	30.0	45.0	34.2
6.076	12.7	25.4	40.0	45.0	31.0
0.256	19.1	25.4	10.0	45.0	88.3
1.017	19.1	25.4	20.0	45.0	70.2
2.282	19.1	25.4	30.0	45.0	62.9
1.711	25.4	50.8	30.0	45.0	48.5
0.763	25.4	50.8	20.0	45.0	64.4
0.192	25.4	50.8	10.0	45.0	93.2
0.384	12.7	50.8	10.0	45.0	87.1
1.525	12.7	50.8	20.0	45.0	55.2
3.423	12.7	50.8	30.0	45.0	36.4

TABLE D.3. Numerical Data for 12" Contraction Fittings.

Stk _c	Outlet I.D. (mm)	Entrance I. D. (mm)	D _p (μm)	Half- Angle (deg.)	P (%)
0.052	6.35	25.4	5.0	12.0	92.0
0.204	6.35	25.4	10.0	12.0	88.8
0.810	6.35	25.4	20.0	12.0	75.3
1.818	6.35	25.4	30.0	12.0	63.4
0.102	6.35	25.4	10.0	12.0	94.2
0.405	6.35	25.4	20.0	12.0	86.1
0.909	6.35	25.4	30.0	12.0	68.3
3.038	6.35	25.4	40.0	12.0	55.1
0.192	6.35	25.4	10.0	12.0	92.2
0.763	6.35	25.4	20.0	12.0	74.0
1.711	6.35	25.4	30.0	12.0	59.2
3.038	6.35	25.4	40.0	12.0	49.9
0.098	12.7	25.4	5.0	12.0	90.3
0.384	12.7	25.4	10.0	12.0	85.6
1.525	12.7	25.4	20.0	12.0	66.9
3.423	12.7	25.4	30.0	12.0	48.0
0.152	12.7	25.4	5.0	12.0	86.3
0.599	12.7	25.4	10.0	12.0	78.2
2.378	12.7	25.4	20.0	12.0	59.7
5.335	12.7	25.4	30.0	12.0	40.4

APPENDIX E
EXPERIMENTAL DATA FOR EXPANSION FITTINGS

TABLE E.1. Experimental Data for 90° Expansion Fittings.

Stk _c	Entrance I.D. (mm)	Outlet I. D. (mm)	D _p (μm)	Half- Angle (deg.)	P (%)	Uncert. (%)
0.039	6.7	27.2	5.7	90.0	69.0	5.9
0.020	6.7	27.2	5.7	90.0	86.3	2.9
0.216	6.7	27.2	5.7	90.0	28.0	3.2
0.131	6.7	27.2	5.7	90.0	29.1	7.7
0.279	6.7	27.2	11.0	90.0	24.8	5.4
0.141	6.7	27.2	11.0	90.0	34.7	15.9
0.071	6.7	27.2	11.0	90.0	53.7	11.4
0.029	6.7	27.2	11.0	90.0	72.6	7.0
0.473	6.7	27.2	11.0	90.0	23.9	17.6
0.782	6.7	27.2	11.0	90.0	31.0	12.1
0.669	6.7	27.2	23.9	90.0	26.2	10.5
0.337	6.7	27.2	23.9	90.0	20.4	3.9
3.712	6.7	27.2	23.9	90.0	63.2	2.7
2.245	6.7	27.2	23.9	90.0	51.0	6.5
0.106	13.0	27.2	5.4	90.0	57.5	2.9
0.045	13.0	27.2	5.4	90.0	84.1	6.3
0.004	13.0	27.2	5.4	90.0	98.6	3.1
0.070	13.0	27.2	10.7	90.0	75.5	5.2
0.035	13.0	27.2	10.7	90.0	86.9	4.1
0.014	13.0	27.2	10.7	90.0	95.1	3.7
0.424	13.0	27.2	10.7	90.0	46.0	2.1
0.239	13.0	27.2	10.7	90.0	47.2	5.9
0.139	13.0	27.2	10.7	90.0	52.4	8.6
0.184	13.0	27.2	24.4	90.0	45.1	4.7
0.904	13.0	27.2	24.4	90.0	53.2	2.5
2.105	13.0	27.2	24.4	90.0	59.6	5.0
0.083	21.0	27.2	21.0	90.0	94.8	1.7
0.488	21.0	27.2	21.0	90.0	83.5	3.2
0.961	21.0	27.2	21.0	90.0	84.4	3.6

TABLE E.2. Experimental Data for 45° Expansion Fittings.

Stk _c	Entrance I.D. (mm)	Outlet I. D. (mm)	D _p (μm)	Half- Angle (deg.)	P (%)	Uncert. (%)
0.039	6.7	27.2	5.7	45.0	65.3	6.9
0.020	6.7	27.2	5.7	45.0	85.8	6.5
0.222	6.7	27.2	5.7	45.0	18.4	10.7
0.131	6.7	27.2	5.7	45.0	21.3	4.3
0.134	6.7	27.2	10.7	45.0	25.3	16.5
0.067	6.7	27.2	10.7	45.0	45.7	14.0
0.027	6.7	27.2	10.7	45.0	73.5	17.7
0.737	6.7	27.2	10.7	45.0	14.5	8.2
0.445	6.7	27.2	10.7	45.0	14.4	5.3
0.268	6.7	27.2	10.7	45.0	15.7	12.3
2.228	6.7	27.2	23.9	45.0	17.4	5.6
3.684	6.7	27.2	23.9	45.0	34.5	18.7
0.334	6.7	27.2	23.9	45.0	18.3	7.4
0.664	6.7	27.2	23.9	45.0	17.2	3.2
0.004	13.0	27.2	5.4	45.0	98.3	3.7
0.045	13.0	27.2	5.4	45.0	79.3	3.7
0.106	13.0	27.2	5.4	45.0	53.8	5.3
0.013	13.0	27.2	10.3	45.0	97.0	4.5
0.207	13.0	27.2	10.3	45.0	46.8	9.9
0.066	13.0	27.2	10.3	45.0	72.8	2.2
0.398	13.0	27.2	10.3	45.0	45.4	8.1
0.207	13.0	27.2	10.3	45.0	46.8	8.1
0.184	13.0	27.2	24.4	45.0	44.4	2.2
0.904	13.0	27.2	24.4	45.0	48.4	4.0
2.105	13.0	27.2	24.4	45.0	53.9	7.4

TABLE E.3. Experimental Data for 12° Expansion Fittings.

Stk _c	Entrance I.D. (mm)	Outlet I. D. (mm)	D _p (μm)	Half- Angle (deg.)	P (%)	Uncert. (%)
0.039	6.7	27.2	5.7	12.0	47.8	6.4
0.020	6.7	27.2	5.7	12.0	83.9	2.2
0.222	6.7	27.2	5.7	12.0	12.0	5.4
0.131	6.7	27.2	5.7	12.0	16.9	3.6
0.254	6.7	27.2	10.5	12.0	11.8	4.4
0.129	6.7	27.2	10.5	12.0	22.8	16.1
0.065	6.7	27.2	10.5	12.0	39.5	19.9
0.026	6.7	27.2	10.5	12.0	75.3	6.7
0.431	6.7	27.2	10.5	12.0	8.5	7.4
0.714	6.7	27.2	10.5	12.0	6.4	12.8
0.664	6.7	27.2	24.4	12.0	6.3	13.5
0.334	6.7	27.2	24.4	12.0	13.5	5.5
3.684	6.7	27.2	24.4	12.0	10.7	7.1
2.228	6.7	27.2	24.4	12.0	8.4	1.9
0.106	13.0	27.2	5.4	12.0	48.6	2.0
0.045	13.0	27.2	5.4	12.0	69.9	2.6
0.004	13.0	27.2	5.4	12.0	96.4	2.0
0.070	13.0	27.2	10.7	12.0	61.0	5.5
0.035	13.0	27.2	10.7	12.0	88.4	4.0
0.014	13.0	27.2	10.7	12.0	92.5	6.3
0.424	13.0	27.2	10.7	12.0	36.7	1.8
0.239	13.0	27.2	10.7	12.0	41.3	3.0
0.139	13.0	27.2	10.7	12.0	45.6	2.7
0.184	13.0	27.2	24.4	12.0	43.0	2.0
1.147	13.0	27.2	24.4	12.0	36.9	10.0
2.117	13.0	27.2	24.4	12.0	39.0	2.1
0.083	21.0	27.2	21.0	12.0	89.0	2.1
0.488	21.0	27.2	21.0	12.0	80.8	2.4
0.961	21.0	27.2	21.0	12.0	81.4	4.6

TABLE E.4. Experimental Data for 6" Expansion Fittings.

Stk _e	Entrance I.D. (mm)	Outlet I. D. (mm)	D _p (μm)	Half- Angle (deg.)	P (%)	Uncert. (%)
0.007	6.7	27.2	5.4	6.0	97.5	1.3
0.085	6.7	27.2	5.4	6.0	24.5	7.5
0.190	6.7	27.2	5.4	6.0	11.4	9.7
0.125	6.7	27.2	10.3	6.0	19.4	5.6
0.024	6.7	27.2	10.3	6.0	80.4	18.4
0.306	6.7	27.2	10.3	6.0	11.6	33.6
0.677	6.7	27.2	10.3	6.0	5.5	13.7
0.472	6.7	27.2	10.3	6.0	9.7	9.2
3.463	6.7	27.2	23.3	6.0	16.0	9.8
1.541	6.7	27.2	23.3	6.0	11.2	23.9
0.316	6.7	27.2	23.3	6.0	13.7	21.7
0.004	13.0	27.2	5.4	6.0	95.1	6.3
0.045	13.0	27.2	5.4	6.0	75.2	4.0
0.106	13.0	27.2	5.4	6.0	55.7	2.2
0.066	13.0	27.2	10.3	6.0	64.8	1.5
0.013	13.0	27.2	10.3	6.0	95.2	3.8
0.207	13.0	27.2	10.3	6.0	49.2	10.3
0.398	13.0	27.2	10.3	6.0	43.2	3.4
0.184	13.0	27.2	24.4	6.0	52.3	5.3
1.147	13.0	27.2	24.4	6.0	39.1	5.7
2.117	13.0	27.2	24.4	6.0	40.6	3.8

TABLE E.5. Experimental Data for 3° Expansion Fittings.

Stk _c	Entrance I.D. (mm)	Outlet I. D. (mm)	D _p (μm)	Half- Angle (deg.)	P (%)	Uncert. (%)
0.085	6.7	27.2	5.4	3.0	31.7	2.9
0.190	6.7	27.2	5.4	3.0	23.7	6.8
0.007	6.7	27.2	5.4	3.0	96.0	4.1
0.677	6.7	27.2	10.3	3.0	13.8	8.1
0.306	6.7	27.2	10.3	3.0	17.3	6.9
0.472	6.7	27.2	10.3	3.0	15.6	11.8
0.125	6.7	27.2	10.3	3.0	26.6	10.1
0.024	6.7	27.2	10.3	3.0	90.4	4.7
0.316	6.7	27.2	23.3	3.0	17.4	13.7
1.541	6.7	27.2	23.3	3.0	18.8	6.8
3.463	6.7	27.2	23.3	3.0	22.7	14.0
0.004	13.0	27.2	5.4	3.0	97.0	1.8
0.045	13.0	27.2	5.4	3.0	86.4	6.0
0.106	13.0	27.2	5.4	3.0	60.8	3.5
0.066	13.0	27.2	10.3	3.0	79.9	3.9
0.013	13.0	27.2	10.3	3.0	91.4	7.0
0.207	13.0	27.2	10.3	3.0	52.1	22.2
0.398	13.0	27.2	10.3	3.0	45.5	2.7
2.117	13.0	27.2	24.4	3.0	42.5	1.5
0.184	13.0	27.2	24.4	3.0	54.8	5.6
1.147	13.0	27.2	24.4	3.0	41.3	3.7
0.083	21.0	27.2	21.0	3.0	91.0	2.4
0.488	21.0	27.2	21.0	3.0	84.6	2.0
0.961	21.0	27.2	21.0	3.0	83.1	2.5

APPENDIX F
EXPERIMENTAL DATA FOR LARGE TRANSPORT TUBES

TABLE F.1. Experimental Data for a 13 mm ID and 2.7 m Long Transport Tube.

Re	Tube I.D. (mm)	Particle Diam. (μm)	P (%)	τ_c	V_c	σ_ϵ	Uncert. (%)
2354	13.0	10.7	91.3	0.971	1.39e-03	1.156	46.2
3901	13.0	10.7	75.7	2.351	4.57e-03	1.029	9.8
7695	13.0	10.7	21.3	7.719	2.76e-02	1.051	15.9
2353	13.0	10.7	89.4	0.971	1.72e-03	1.060	20.7
3387	13.0	10.7	79.8	1.836	3.61e-03	1.110	34.7
4669	13.0	10.7	44.4	3.220	1.45e-02	1.048	15.2
5942	13.0	10.7	24.2	4.911	2.53e-02	1.069	21.6
7696	13.0	10.7	15.7	7.721	3.30e-02	1.038	11.9
3901	13.0	6.2	90.3	0.812	1.67e-03	1.047	17.4
5935	13.0	6.2	74.3	1.694	5.13e-03	1.055	17.1
9651	13.0	6.2	28.5	3.965	2.30e-02	1.069	21.3
8189	13.0	6.2	41.0	2.971	1.60e-02	1.047	14.5
6694	13.0	6.2	59.2	2.088	9.18e-03	1.042	13.1
4669	13.0	6.2	89.3	1.111	1.66e-03	1.890	181.9

TABLE F.2. Experimental Data for a 26 mm ID and 2.7 m Long Transport Tube.

Re	Tube I.D. (mm)	Particle Diam. (μm)	P (%)	τ_+	V_+	σ_s	Uncert. (%)
62225	26.0	10.2	5.6	67.022	1.34e-01	1.013	4.2
14334	26.0	10.2	62.8	5.134	1.79e-02	1.055	17.1
6290	26.0	10.2	93.3	1.215	2.43e-03	1.012	14.9
2598	26.0	10.2	98.5	0.259	4.62e-04	1.290	98.1
14265	26.0	20.0	6.2	19.552	1.07e-01	1.014	4.4
13290	26.0	20.0	7.4	17.273	9.93e-02	1.050	15.6
11228	26.0	20.0	15.6	12.859	6.95e-02	1.010	3.2
8784	26.0	20.0	30.3	8.369	4.34e-02	1.028	8.7
6070	26.0	20.0	67.6	4.384	1.49e-02	1.125	39.4
5830	26.0	20.0	80.2	4.085	5.46e-03	1.483	95.8
9563	26.0	11.8	65.4	3.458	7.76e-03	1.078	23.5
8734	26.0	11.8	72.3	2.951	5.88e-03	1.024	8.2
6949	26.0	11.8	80.0	1.978	3.93e-03	1.040	13.2
5086	26.0	11.8	88.6	1.145	2.04e-03	1.104	32.8

TABLE F.3. Experimental Data for a 52 mm ID and 2.7 m Long Transport Tube.

Re	Tube I.D. (mm)	Particle Diam. (μm)	P (%)	τ_+	V_+	σ_g	Uncert. (%)
6209	52	20.0	91.2	1.221	6.40e-03	1.036	15.6
16705	52	20.0	65.7	6.444	3.29e-02	1.024	8.0
25047	52	20.0	37.6	13.091	8.08e-02	1.119	35.7
39351	52	20.0	18.8	28.862	1.46e-01	1.031	9.7
55311	52	20.0	16.7	52.370	1.63e-01	1.016	5.2
6605	52	10.2	99.3	0.336	4.66e-04	1.319	164.9
19970	52	10.2	91.0	2.331	7.56e-03	1.139	40.7
34221	52	10.2	61.2	5.983	4.22e-02	1.020	6.6
49845	52	10.2	42.4	11.554	7.73e-02	1.051	15.9
68767	52	10.2	29.8	20.292	1.14e-01	1.022	7.0
36946	52	10.8	47.3	7.745	6.45e-02	1.021	7.0
49973	52	10.8	37.1	13.139	8.93e-02	1.014	5.4
9647	52	10.8	97.5	0.739	1.82e-03	1.267	84.3
25002	52	10.8	70.1	3.911	2.83e-02	1.084	7.3
12454	52	10.8	95.9	1.155	3.15e-03	1.196	61.0
27849	52	10.8	68.6	4.723	3.15e-02	1.046	14.5
39384	52	10.8	50.0	8.662	6.06e-02	1.057	17.9
62272	52	10.8	31.7	19.310	1.06e-01	1.015	4.7

TABLE F.4. Experimental Data for a 102 mm ID and 5.5 m Long Transport Tube.

Re	Tube I.D. (mm)	Particle Diam. (μm)	P (%)	τ_+	V_+	σ_g	Uncert. (%)
24118	102.0	10.8	92.4	0.983	7.41e-03	1.206	65.9
29208	102.0	10.8	90.1	1.374	8.51e-03	1.280	75.3
31136	102.0	10.8	88.1	1.537	1.07e-02	1.093	29.2
32951	102.0	11.8	86.2	2.017	1.26e-02	1.139	42.3
24909	102.0	11.8	93.4	1.236	5.64e-03	1.102	34.7
19692	102.0	11.8	94.5	0.819	4.54e-03	1.045	22.7
9846	102.0	11.8	97.7	0.244	1.81e-03	1.339	99.1
25976	102.0	17.7	75.5	2.930	2.24e-02	1.483	110.1
21840	102.0	17.7	88.2	2.163	9.05e-03	1.311	79.5
17723	102.0	17.7	92.3	1.501	4.23e-03	1.594	104.1
31508	102.0	20.0	59.3	5.236	4.44e-02	1.035	11.0
19692	102.0	20.0	79.7	2.300	1.70e-02	1.143	38.6
13925	102.0	20.0	90.3	1.254	7.84e-03	1.098	30.8
6707	102.0	20.0	98.0	0.349	1.40e-03	1.083	56.2

VITA

Name: Arnoldo Muyshondt

Date & Place
of Birth: February 12, 1964
Rochester, New York

Permanent
Address: Department of Mechanical Engineering
Texas A&M University
College Station, Texas 77843

Education: B. S. in Mechanical Engineering (August 1986),
Texas Tech University,
Lubbock, Texas.

M. S. in Mechanical Engineering (May 1988),
Texas Tech University,
Lubbock, Texas.

Ph. D. in Mechanical Engineering (December 1995),
Texas A&M University,
College Station, Texas.

Work
Experience: 8/92 - 12/95 Graduate Research Assistant,
Aerosol Technology Lab.,
Texas A&M University,
College Station, Texas.

5/88 - 7/92 Senior Engineer,
General Dynamics,
Fort Worth, Texas.

8/86 - 5/88 Graduate Research Assistant,
Texas Tech University,
Lubbock, Texas.